UNIVERSIDADE FEDERAL DO RIO GRANDE DO SUL
ESCOLA DE ENGENHARIA
PROGRAMA DE PÓS-GRADUAÇÃO EM ENGENHARIA DE MINAS,
METALÚRGICA E DE MATERIAIS

LUIS FERNANDO KANAN

FRICTION HYDRO-PILLAR PROCESSING OF CARBON STEELS:
A numerical investigation of joint structure, properties and material flow

Porto Alegre
2023

LUIS FERNANDO KANAN

FRICTION HYDRO-PILLAR PROCESSING OF CARBON STEELS:
A numerical investigation of joint structure, properties and material flow

Thesis submitted to the Post Graduation Program in Mining, Metallurgy and Materials (PPGE3M) from Federal University of Rio Grande do Sul (UFRGS) as part of the requirements for obtaining the title of Doctor of Philosophy in Engineering.

Advisor: Prof. Dr. Thomas Gabriel Rosauro Clarke

Porto Alegre
2023

LUIS FERNANDO KANAN

SOLDAGEM POR FRICÇÃO COM PINO CONSUMÍVEL EM AÇO CARBONO:
Uma investigação numérica sobre união, propriedades e fluxo de material

Tese submetida ao Programa de Pós-Graduação em Engenharia de Minas, Metalúrgica e de Materiais da Universidade Federal do Rio Grande do Sul, como requisito parcial à obtenção do título de Doutor em Engenharia, modalidade Acadêmica

Orientador: Prof. Dr. Thomas Gabriel Rosauro Clarke

Porto Alegre
2023

Kanan, Luis Fernando
FRICTION HYDRO-PILLAR PROCESSING OF CARBON STEELS: A numerical investigation of joint structure, properties and material flow / Luis Fernando Kanan. -- 2023.
85 f.
Orientador: Thomas Gabriel Rosauro Clarke.

Tese (Doutorado) -- Universidade Federal do Rio Grande do Sul, Escola de Engenharia, Programa de Pós-Graduação em Engenharia de Minas, Metalúrgica e de Materiais, Porto Alegre, BR-RS, 2023.

1. Soldagem por fricção. 2. Friction hydro-pillar processing. 3. Simulação numérica. 4. Distribuição de dureza. 5. Fluxo de material. I. Rosauro Clarke, Thomas Gabriel, orient. II. Título.

ACKNOWLEDGEMENTS

Many helped with the development of this work. Even though I would like to give proper recognition to all of those who gave their time and attention, it would be a tough task. However, some of the major contributions should be mentioned.

To my advisor prof. Thomas Gabriel Rosauro Clarke for actively giving support and insight through all stages of this work.

To prof. Buchibabu Vicharapu and prof. Amitava De from the Indian Institute of Technology Bombay who started as partners in the development of this work and later became friends.

To Dr. Renan Landell and MSc. Diogo Buzzatti for playing a very important part in the experiments and analysis. This work could not have been done without their contributions.

To my colleagues in the post-graduation program in Science and Technology of Materials (PPGE3M) and in the Physical Metallurgy Laboratory (LAMEF), in special to my group PROENG.

To Msc. Fabiano Mattei, who gave me direction and paved the way through all phases of my technical development.

To the late prof. Telmo Roberto Strohaecker, for giving me the opportunity to work in one of the best research facilities that I know of, a place which I used to call my second home.

To my family, Ana Paula Aquistapase Dagnino, Rosmarie Bertolucci Kanan, Luis Felipe Correa Kanan, Manuela Kanan, Hector Rodolfo Dagnino Moyano and Graciela Aquistapase Dagnino, for all their love, companionship and emotional support.

To the Brazilian governmental agency “Conselho Nacional de Desenvolvimento Científico e Tecnológico (CNPq)”, Petrobras and ANP (Brazilian Agency for Petroleum and Energy) for sponsoring this research.

RESUMO

A Soldagem por Fricção com Pino Consumível (Friction Hydro Pillar Processing - FHPP) é uma técnica inovadora de união em estado sólido utilizada para reparar componentes de parede espessa. Durante o processo, o pino é rotacionado contra uma cavidade usinada no local do defeito para induzir aquecimento por fricção e fluxo do material plastificado para preenchimento adequado. Este trabalho apresenta uma investigação abrangente do FHPP, com foco na relação das variáveis de processo com a microestrutura, propriedades da junta, e fluxo do material. Buscando uma compreensão mais profunda e otimização dessa técnica de soldagem, três estudos foram realizados em diferentes tipos de aço, com uma abordagem conjunta experimental e numérica.

No primeiro estudo, foram examinados os efeitos das variáveis do processo na microestrutura e nas propriedades da junta resultante, ou seja, estudou-se como a força, a velocidade de rotação do pino e o tempo de processamento, influenciam na obtenção da junta soldada por FHPP no aço ASTM A36. Um modelo numérico foi desenvolvido para examinar a taxa de geração de calor, o campo de temperatura transiente e sua correlação com as variáveis de processamento. A partir da análise experimental e numérica foi possível desenvolver um método para estimar a distribuição de dureza das juntas. Baseando-se no estudo anterior, o segundo artigo de pesquisa foca no FHPP de aço AISI 4140. Os resultados enfatizam a importância da otimização da taxa de força do pino e do tempo de processamento para obter juntas livres de defeitos e preenchimento adequado de furos de trincas.

O terceiro estudo aborda o fluxo de material durante o FHPP, um aspecto pouco relatado na literatura. Por meio de uma combinação de análise teórica e experimentos de tomografia computadorizada por raios-x tridimensionais (XCT), utilizou-se um inserto de liga de titânio para rastrear o fluxo de material durante o FHPP de um substrato AISI 4140. Um modelo numérico termomecânico axissimétrico foi desenvolvido para rastrear o fluxo do material. Os resultados mostraram que a porção central do pino se deforma em uma série de planos de cisalhamento em camadas, enquanto que o material plastificado mais externo radialmente flui pela folga entre o pino e a peça, com o excesso de volume sendo expulso como rebarba.

Palavras-chave: Soldagem por fricção; Friction hydro-pillar processing; Aço; Análise de transferência de calor; Distribuição de dureza; Simulação numérica; Fluxo de material.

ABSTRACT

Friction hydro-pillar processing (FHPP) is a solid-state joint technique employed for repairing thick-walled components using an external stud. During the process, the stud is rotated against a crack-hole to induce friction heating and flow of plasticized material for proper filling. This Ph.D. thesis presents a comprehensive investigation of FHPP, focusing on the determination of joint structure, material flow, and properties while considering the effects of processing variables. Contributing to a deeper understanding and optimization of the technique, three critical studies were carried out on different types of steel substrates with a joint experimental and numerical approach.

The first study investigates the effect of processing conditions - such as stud force, rotational speed and processing time - on joint structure and properties in FHPP of ASTM A36 steel. A numerical model was developed. in which the rate of heat generation, transient temperature field, and their correlation with processing variables were examined. From experimental and numerical analyses results, a method to estimate the hardness distribution within the joints was presented. Building upon the previous study, the second research paper focuses on FHPP of AISI 4140 steel. The results emphasize the importance of optimizing stud force rate and processing time to achieve defect-free joints and proper filling of crack holes, offering valuable insights into the systematic and quantitative aspects of the technique.

The third study addresses the material flow during FHPP, an aspect that is often underreported in the literature. Through a combination of theoretical analysis and three-dimensional X-ray computer tomography (XCT) experiments, a Ti-alloy tracer material was used to track material flow during FHPP of an AISI 4140 substrate. A thermo-mechanical axi-symmetric numerical model was developed to further investigate and track the material flow. The findings reveal stationary layer-wise shear planes in the central portion of the plug and flow of plasticized material from the tapered interface through the clearance between the plug and the substrate, with excess volume being extruded as flash.

Keywords: Friction welding; Friction hydro-pillar processing; Steel; Heat transfer analysis; Hardness distribution; Material flow; Numerical simulation.

LIST OF FIGURES

LIST OF TABLES

SUMMARY

1 INTRODUCTION

Friction Hydro Pillar Processing (FHPP) is a solid-state joining process developed by TWI (THOMAS *et al.*, 1993) whose main feature is its ability to repair cracks in thick elements. The process consists of machining a hole with a specific geometry, removing the defect, and then introducing a pin subjected to force and rotation. Initially, the friction between the pin and the base of the hole generates enough heat to allow the applied load to plastically deform the parts. Heat generation increases with increasing plastic deformation, causing the pin to conform to fill the existing void. The process ends with the expulsion of material in the form of flash and subsequent machining to remove the spare material (MEYER, 2003; NICHOLAS, 2003).

Even though FHPP has been around since 1993, it is still lacking in detailed studies in the literature (BULBRING *et al.*, 2013; MEYER, 2003). Better understanding of thermal and strain history of the material are key features to ensure good bonding and good mechanical properties The process presents challenges in terms of monitoring the temperature and material flow during the process, which are essential variables for this. One of the most recently exploited resources in the technological development of this process is computational analysis.

This thesis is written in an article presentation format, in which three published articles are presented as the scope of this research. It is organized with a brief introduction on the process characteristics, available studies and objectives, followed by an article integration chapter, in which their main findings are discussed. After the integration, the full articles are presented, followed by concluding remarks and references.

1.1 APPLICATIONS

As a solid-state process, FHPP shows great potential with difficult-to-weld materials, such as high-carbon and alloy steels. Pressure vessels, forging dies, ship hulls and power plants are a few examples of possible applications. Because it is an automated process, it can be used in highly hazardous environments, such as a submerged, radioactive and/or explosion-threatening conditions. FHPP offers advantages over traditional welding methods, such as avoiding problems associated

with melting, porosity, hydrogen embrittlement, and residual stresses. Combining these characteristics, the process is interesting for several industries, such as naval, space, oil and nuclear (AMAVISCA C. V., 2019; BULBRING *et al.*, 2013; HOWSE; LUCAS; THOMAS, 2002; NICHOLAS, 2003; PAULY *et al.*, 1998). A list of the main advantages of FHPP can be seen on Table 1.1.

Table 1.1 FHPP advantages.

FHPP ADVANTAGES
No filler metal, flux or shielding gas are required.
Safer for operators and environmentally cleaner than conventional arc welding. Generally, no arcs, smoke or fumes are generated during friction welding processes.
It's an automated process, thus operators do not require special training and the process is suitable for hazardous environment applications.
Can be performed underwater, making it a great process for ROV sea operations
It's a solid-state process, not being subjected to problems associated to melting and solidification phenomena. Has potential for materials with conventional arc welding restrictions, such as tool steels.
Usually faster than conventional arc welding processes.
The joint usually presents higher strength than base material.
It is suited for joining dissimilar metal combinations.
If performed in sequence, as its "stich welding" variant, the process can be applied in a bigger set of problems, such as filling a crack path.

Source: (AMAVISCA C. V., 2019; AMERICAN WELDING SOCIETY, 1991, p. 749; LANDELL *et al.*, 2019; MEYER, 2003).

Despite the significant advantages, some limitations must also be acknowledged (Table 1.2). One such aspect is the high dependency on accurate process control. Precise adjustment of parameters such as the stud force, rotational speed, and processing time is critical to achieve a defect-free joint and optimal hole filling. Another limitation lies in the high residual stresses and presence of defects like voids, especially if the process parameters are not meticulously controlled. While FHPP holds promise as a potent repair technique for thick metal components, continued exploration and understanding of its limitations and their solutions is essential for broadening its applicability, efficiency, and overall effectiveness.

Table 1.2 FHPP limitations.

FHPP LIMITATIONS
Relatively new process, thus having scarce literature information.
Processing parameters and control dependence
Equipment and tooling are more expensive than general welding equipment.
Usually requires machining before and after process.
Impurities from stud/substrate initial interface won't be expelled with flash, showing the need of careful cleaning of the parts.
Geometry is limited to axi-symmetric angular or flat forms.

Source: (AMERICAN WELDING SOCIETY, 1991, p. 749; LANDELL *et al.*, 2019; MEYER, 2003).

1.2 GEOMETRY

FHPP initially utilized straight cylindrical shaped studs, but they showed inadequate mixing and lack of coalescence with the substrate. Subsequent studies introduced tapered studs, which improved crack volume filling and consolidation processes. Pre-machining the cracks with chamfered edges also reduced bonding defects. The selection of appropriate processing conditions, such as rotational speed, axial force, and burn-off length, proved critical in achieving optimal joint properties (BULBRING *et al.*, 2013; HATTINGH *et al.*, 2011, 2015; MEYER, 2003; YIN* *et al.*, 2015; YIN *et al.*, 2015).

1.3 NUMERICAL METHODS

The numerical modeling of FHPP plays a pivotal role in advancing this innovative solid-state joining process and unlocking its full potential. By using numerical methods such as finite element analysis (FEA) and computational fluid dynamics (CFD), researchers and engineers can gain deep insights into the complex thermo-mechanical phenomena involved in FHPP. These simulations allow for the visualization and prediction of temperature distributions, material flow patterns, and stress distributions during the process. The ability to model FHPP facilitates the optimization of process parameters, such as rotational speed, axial pressure, and tool geometry, to achieve superior joint quality and structural integrity while minimizing defects and material waste. Moreover, numerical modeling provides a cost-effective and time-efficient approach to explore various design modifications and investigate

the influence of different materials on the FHPP process. Overall, the importance of numerical modeling in FHPP lies in its ability to enhance process understanding, optimize parameters, and guide future advancements, ultimately leading to the successful application of this process in industries where large-scale, high-strength joints are critical. Some of the works that used numerical methods associated with FHPP can be seen on Table 1.3.

Table 1.3 Numerical methods on FHPP.

Author	Description
UNFRIED S. *et al.*, (2010)	Used thermodynamic numerical analysis to describe the microstructural evolution of friction taper plug welded joints of C–Mn steels by relating experimental temperature history and chemical composition with calphad method calculation and continuous cooling transformation data.
XU *et al.*, (2015)	Developed a thermomechanical numerical model to evaluate the partial filling of various stud and substrate geometries during the initial stage of FHPP of C–Mn steel.
(KANAN *et al.*, 2018; VICHARAPU *et al.*, 2017)*	Developed a heat transfer model accounting for material movement and volume-based heat generation of ASTM A36 and AISI 4140 steels FHPP, with subsequent hardness estimation from cooling rates derived from the numerical analysis.
LI *et al.*, (2018)	Developed a heat generation model designed to account for movement and deformation of the friction welding interface for Q345 steel FHPP. The authors calculated the cooling rate at specific points and correlated it with continuous cooling curves to estimate the formed phases.
LESSA et al., (2019)	Performed thermodynamic numerical analysis to evaluate phase formation from temperature measurements acquired during FHPP of AID SAF 2205.
AMAVISCA C. V., (2019)	Evaluated the residual stresses of H13 steel FHPP using X-ray analysis and the contour method. The contour method is a destructive technique that combines a three-dimensional measurement of a cut part and subsequent FEM analysis to calculate it's residual stresses (PRIME, 2001).
(LANDELL *et al.*, 2019)*	Developed fully coupled thermomechanical FHPP model for material flow analysis of AISI 4140 steel. The authors were able to track the material flow and determine which portion was expelled through flash.

Source: Author.

1.4 OBJECTIVES

This work aims to investigate the joint structure, properties and material flow of Friction Hydro Pillar Processing of ASTM A36 and AISI 4140 steels through numerical

methods associated with experimental tests. During the course of this research, three articles were published, each with its own specific objectives: Figure 1.1 depicts the main and specific objectives of this work, illustrating the evolution of experimental test design and numerical methods.

Figure 1.1 - Main and specific objectives.

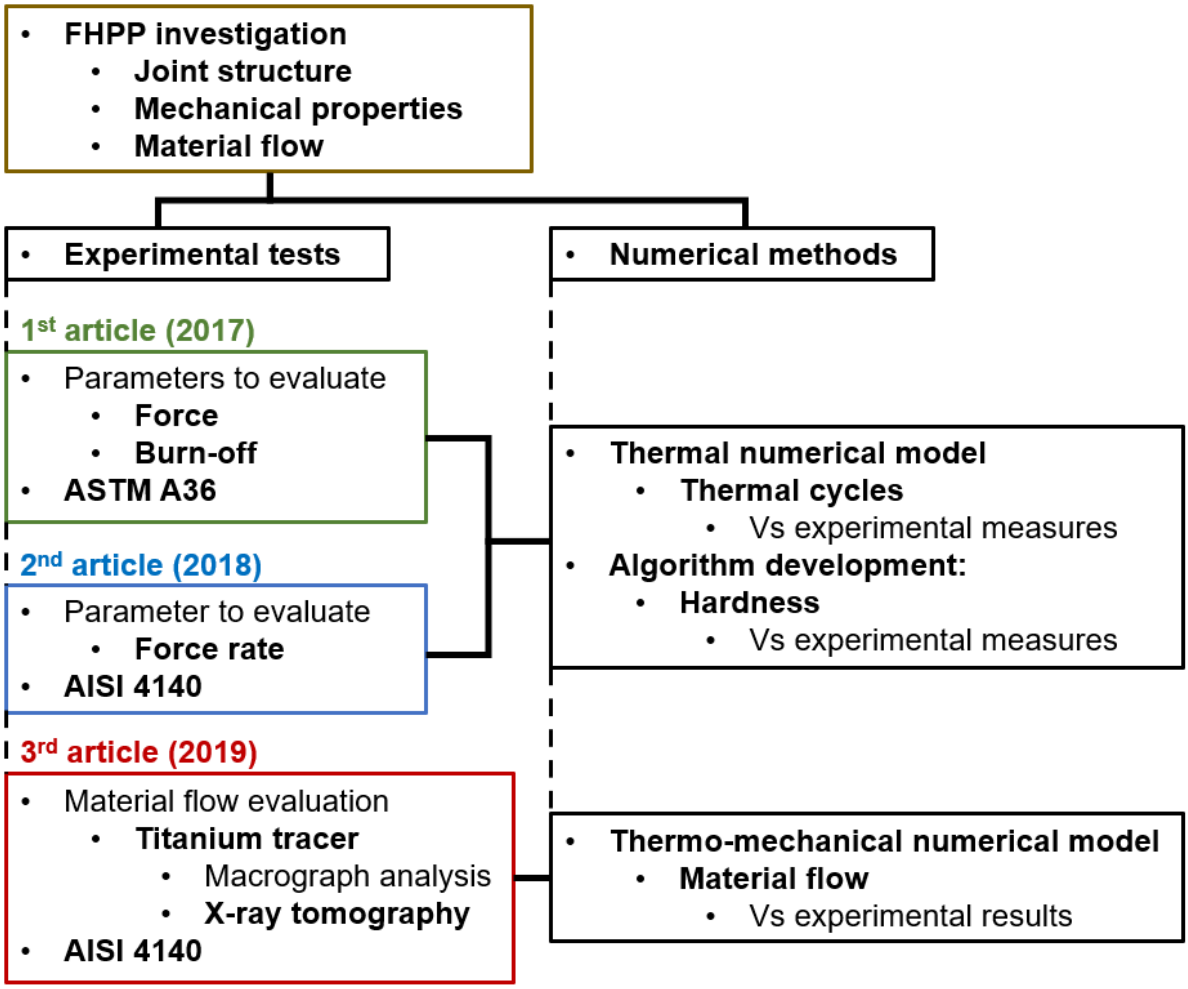

Source: Author.

1.4.1 Specific objectives

The first article (chapter 3) objective was to comprehend the friction hydro-pillar processing method and its application on ASTM A36 steel and to define the underlying relationship between processing conditions and the joint's structure and properties.

- Evaluate the influence of welding force and burn-off parameters in FHPP of ASTM A36 steel;

- Develop a simplified numerical model to investigate the thermal cycles of the process and compare its calculated results with experimental measurements;
- Develop an algorithm to estimate the hardness mechanical property and verify its representativeness against experimental measurements;

The second article (chapter 4) aims to expand the scope of the first article by applying it to AISI 4140 steel, a medium carbon steel, focusing to establish a correlation between processing variables (stud force, rotational speed, total processing time) and the joint's structure and properties.

- Evaluate the influence of the force rate parameter in FHPP welding of AISI 4140 steel;

The third article (chapter 5) aimed to provide detailed insights into material flow dynamics during the FHPP process

- Evaluate the material flow during FHPP welding of AISI 4140 steel using titanium tracer and computed tomography;
- Develop a thermo-mechanical numerical model to investigate the material flow during welding and evaluate its representativeness against experimental results.

The works elaborated and carried out during this thesis were developed at the Physical Metallurgy Laboratory (LAMEF-UFRGS) in partnership with the Indian Institute of Technology Bombay. This work was supported by Department of Science and Technology, Ministry of Science and Technology: [Grant Number INT/BRAZIL/P-14/2013]; CNPq: [Grant Number 401014/2013-4].

2 INTEGRATION OF SCIENTIFIC ARTICLES

This work consists of the integration of three articles on Friction Hydro Pillar Processing (FHPP). Methods associating experimental tests and numerical models were used in all works, where tools to investigate thermal cycles, mechanical properties and material flow during FHPP were developed. The relationship between the published papers can be seen in Figure 1.1. The first work aims to develop a methodology for studying thermal cycles and resulting properties of the FHPP process while the second work implements and further discuss this method in a different material. The third work completes the investigation of the previous welding focused on a different but equally important feature: the material flow during processing. The following sections present a short explanation of the papers and their achievements.

2.1 AN INVESTIGATION ON FRICTION HYDRO-PILLAR PROCESSING (2017)

The first article examines the FHPP technique applied to ASTM A36 steel. The purpose was to understand the fundamentals of the process and analyze the joint structure and properties in this type of steel. Through a combination of experimental and numerical methods, a better understanding of the process and its applicability was achieved.

Three welding parameters were tested, with differences in welding strength and burn-off. The temperature was monitored during each weld at three positions per sample. Samples were cut and macrographs and hardness profiles were taken for analysis.

Furthermore, an axisymmetric numerical model was developed using the Finite Element Method from ABAQUS software (DASSAULT SYSTÈMES SIMULIA CORP., 2014). The model uses a thermal approach and works from the sequential activation of predefined volumes for heat generation. The model was used to calculate the temperature variation at the same experimentally monitored points, showing consistency with the results.

An algorithm for hardness prediction was developed, having as input data the thermal history and the chemical composition of the steel. The numerical model allowed to calculate the thermal cycle in the same measurement positions of the hardness profiles of the samples. These temperature curves were then used in

conjunction with the hardness prediction algorithm and showed calculated hardness values similar to those measured experimentally.

The key findings of the first article include:

- The successful application of FHPP on ASTM A36 steel;
- The importance of proper processing conditions for effective joint formation;
- The development of a method to estimate material properties.

2.2 FRICTION HYDRO-PILLAR PROCESSING OF A HIGH CARBON STEEL: JOINT STRUCTURE AND PROPERTIES (2018)

In the second article, the study delves deeper into the FHPP process, focusing on AISI 4140 steel, a high carbon steel variant. By employing a similar approach of experimental and theoretical methodologies, the article analyses the effect of various processing variables on the joint structure and properties.

Three welding parameters for AISI 4140 steel were evaluated, in which only the force rate was varied. This variation resulted in different welding times and in changes of the thermal profile. Welding with the lowest force rate showed the best result, with a weld free of defects.

The numerical model and hardness prediction algorithm developed in the previous article were modified to consider the change of parameters and geometrical and material differences between the works. The calculated results were similar to those measured experimentally, with the hardness calculated at the base of the sample as the most discrepant result, possibly due to grain refining, which was not taken into account in the algorithm.

Some of the key findings from the second article are:

- The successful application of FHPP on AISI 4140 steel;
- A deeper understanding of processing variables, in special the rate of applied force, and their impact on joint formation;
- The verification of the method developed in the first article for hardness estimation.

2.3 MATERIAL FLOW DURING FRICTION HYDRO-PILLAR PROCESSING (2019)

The third article explores the largely uncharted domain of material flow dynamics during the FHPP process. Through the incorporation of a Ti-alloy tracer material within an AISI 4140 steel substrate, cutting-edge analysis techniques such as three-dimensional X-ray computer tomography were employed to scrutinize the material flow and its relationship with the joint structure.

One welding parameter on AISI 4140 steel was tested. The studs used for welding were specially prepared with titanium inserts in different positions, which made it possible to visualize the presence or absence of titanium in sample sections. In addition, the computed tomography of samples allowed a three-dimensional visualization of titanium in contrast to steel. These results indicated that the material in the central part of the stud stays in the base of the weld, while the material in the periphery of the pin is expelled with the flash.

A thermo-mechanical axisymmetric numerical model was developed with ABAQUS software (DASSAULT SYSTÈMES SIMULIA CORP., 2012) to calculate the material flow during the process. The main difference between this model and the previous ones is that it considers thermal and structural elements, not just thermal ones. In this way, the model becomes capable of calculating deformations from localized stress fields, effectively reproducing the gap filling between stud and substrate and flash formation.

The model results were used to calculate the trajectory of points positioned in the same regions as the inserts, which presented results in accordance to the experimental ones. Furthermore, the calculated peak temperature, final geometry and flash volume were also similar to those measured experimentally.

The key findings from the third article include:

- Unveiling underlying material flow dynamics during the process
- Gaining insights into the effect of material flow on the joint structure
- The innovative use of Ti-alloy tracers to observe and analyze material flow dynamics.

3 AN INVESTIGATION ON FRICTION HYDRO-PILLAR PROCESSING

V. Buchibabu[1], L. F. Kanan[2], T. Clarke[*2] and A. De[1]

[1]Indian Institute of Technology Bombay, India
[2]Universidade Federal do Rio Grande do Sul (UFRGS), Porto Alegre, Brazil
(*Corresponding author: tclarke@demet.ufrgs.br)

Science and Technology of Welding and Joining
Volume 22, Jan 2017, p. 555-561.
https://doi.org/10.1080/13621718.2016.1274849

Abstract

Friction hydro pillar processing is a novel technique to fill in crack-holes in thick-walled metal structures by an external stud and forming a solid-state bond between the stud and the metal substrate. During the process, the stud is rotated against the crack-wall to facilitate friction heating and flow of plasticized material for proper filling of the crack-hole. We present here a coupled experimental and numerical study on friction hydro pillar processing of ASTM A36 steel to understand the effect of processing conditions on the joint structure and properties. An axi-symmetric heat transfer analysis is carried out to compute the temperature field. The computed thermal cycles are used to estimate the hardness distribution across the joint. The estimated thermal cycles and hardness distribution are tested with the corresponding experimentally measured results.

Keywords: Friction hydro pillar processing; Steel; Heat transfer analysis; Hardness distribution; Friction welding; Numerical simulation.

3.1 INTRODUCTION

Friction hydro pillar processing (FHPP) is a novel solid-state joining process that has attracted wide attention for repairing of cracks in thick-walled steel vessels (HARTLEY, 2000; HATTINGH *et al.*, 2016; NICHOLAS, 2003; THOMAS; NICHOLAS, 1992). Figure 3.1 shows three sequential stages in FHPP (CHLUDZINSKI *et al.*, 2012; YEH *et al.*, 2013) and the attached video file shows a complete weld being performed. The process starts with a dwell stage as an external rotating stud is pressed into a crack-hole, which is pre-machined to fully open the existing crack, leading to frictional heating along the stud-hole interface. Next, the rotating stud is forced into the crack-hole resulting in plastic flow of stud material through the stud-hole clearance, which is referred to as the burn-off stage. As the crack-hole is completely filled up, the rotational motion of the stud is stopped and the force is increased to promote a solid-state bond between the stud and substrate that is defined as the forging stage. The structure and properties of the final joint are significantly affected by the alloy properties and the processing conditions such as force, rotational speed and geometry of the stud and the hole (BULBRING *et al.*, 2013; CHLUDZINSKI *et al.*, 2012; HATTINGH *et al.*, 2011, 2015; MEYER, 2003; YIN* *et al.*, 2015; YIN *et al.*, 2015).

Figure 3.1 - Schematic diagram showing (a) dwell stage, (b) burn-off stage and (c) forging stage of the friction hydro pillar processing (FHPP).

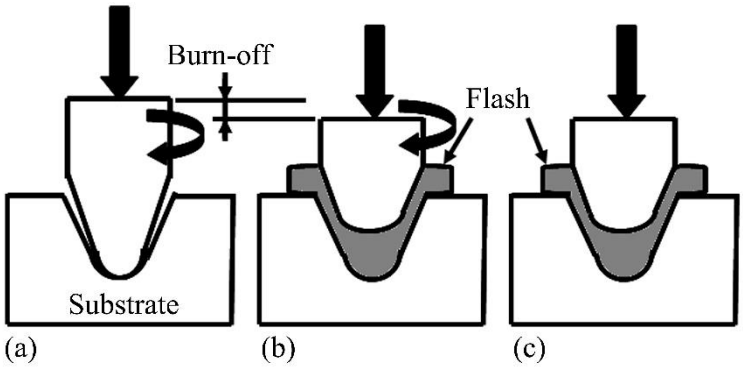

Source: Author.

Since FHPP is a relatively new process, detailed studies are scarce in the open literature. The shape of the pre-machined hole and that of the stud are considered to be important in FHPP. Straight and tapered cylindrical shaped studs were commonly attempted with the latter found to be more efficient in easing the flow of plasticized material and producing defect free joints (BULBRING *et al.*, 2013; HATTINGH *et al.*,

2011, 2015; MEYER, 2003; YIN* *et al.*, 2015; YIN *et al.*, 2015). Meyer (2003) and Hattingh et al. (2015) reported that tapered cylindrical shaped holes eased the flow of plasticized stud material. Meyer (2003) and Xu et al. (XU *et al.*, 2015) showed that the pre-machined holes with chamfered edges eliminated defects such as lack of filling. In contrast, sharp edges at the bottom of the hole resulted in stress concentration and void like defects.

The force on the stud and its rotational speed during dwell time and burn-off stage contribute to the frictional heating along the stud-hole interface, and thermal softening and flow of plasticized stud materials. Chuldzinski et al. (CHLUDZINSKI *et al.*, 2012) reported that rise in stud force from 50 to 400 kN in the burn-off stage reduced the processing time from 30 to 2 s, which also lowered the peak temperature from 1535 to 838 K. Hattingh et al. (2011) noted similar phenomena in FHPP of 10CrMo910 and AISI 4140 steels. Yeh et al. (2013) argued that an adequate time was needed during burn-off stage for proper consolidation of FHPP joints. For example, a stud force of 350 kN during burn-off stage resulted in incomplete bonding in FHPP of C-Mn steel plates while defect free joints were obtained at a smaller force of 200 kN and higher processing time(MEYER, 2003; YEH *et al.*, 2013). In FHPP of X65 pipe steels, Meyer (2003) found adequately bonded joints with a narrow heat affected zone (HAZ) at a stud rotational speed of 2000 rpm. The joint quality deteriorated as the stud rotational speed was increased further to 8000 rpm (YIN* *et al.*, 2015). Although these studies exhibited the importance of processing conditions in FHPP, their influence on the thermal cycles and the joint property was not studied in a systematic manner.

A quantitative knowledge of peak temperature and thermal cycles could provide a measure of the joint properties during welding of alloys (KOU, 1987). Real-time monitoring of temperature at the stud-hole interface is difficult in FHPP due to the flow of plasticized material. Xu et al. (XU *et al.*, 2015) used finite element based numerical model to analyze the heat transfer and material flow in FHPP of C-Mn steel. The computed peak temperature at the joint interface was around 1593 K for a stud rotational speed of 7000 rpm and force of 20 kN. Although such model can provide an insightful understanding, very little work on process modelling of FHPP is reported in open literature.

A coupled experimental and theoretical study on FHPP of ASTM A36 steel was therefore undertaken in the current work. A three-dimensional transient heat transfer analysis was carried out with simplified assumptions to account for the filling of the

crack-hole by the external stud material in discrete time-steps. The computed thermal cycles were validated extensively with the corresponding experimentally measured results at pre-set monitoring locations for a range of conditions. An attempt was finally made to relate the computed thermal cycles with the measured hardness distribution across the FHPP joints.

3.2 EXPERIMENTAL PROCEDURE

Experiments were conducted using a force controlled FHPP machine at LAMEF-UFRGS, Brazil (CHLUDZINSKI *et al.*, 2012; YEH *et al.*, 2013). Table 3.1 depicts the chemical composition of the stud and substrate alloys. Table 3.2 shows the processing conditions used here. Figure 3.2(a) and (b) show the stud-hole geometry used for the experiments. Three commercial grade K-type thermocouples with thermal resistant sheathing were used to measure the thermal cycles close to the joint at a simultaneous sampling rate of 20 Hz. Each thermocouple was fixed into a small hole of diameter 3±0.25 mm by capacitor discharge welding. Prior to fixing, each thermocouple was calibrated according to ASTM E230/E230M (2017) and the average error in measurement during calibration was found well within ± 2.5°C. Figure 3.2(c) shows the locations of the thermocouples, TC1, TC2 and TC3 at 7.5, 15 and 22 mm below the substrate surface, respectively. Each thermocouple was located around 1.5±0.5 mm away from the original boundary of the pre-machined hole. All the joined coupons were sectioned transversely along the symmetry plane to perform the microscopy analysis with 10% nital etchant. Figure 3.2(c) also shows the locations for the measurement of Vickers micro-hardness on joint transverse cross-section. The micro-hardness was measured using a load of 0.3 kg and holding time of 10 s.

Table 3.1 - Chemical composition (in Wt%) of ASTM A36 steel.

	C	**Si**	**Mn**	**P**	**S**	**Cr**	**Mo**	**Ni**	**Al**
Substrate	0.134	0.175	0.914	0.0175	0.0125	<0.001	<0.005	<0.005	0.0185
Stud	0.149	0.144	0.842	0.0161	0.015	<0.001	<0.005	<0.005	0.0165

Source: Author.

Table 3.2 - FHPP conditions considered in this work.

Stud rotational speed (rpm)	1500
Stud burn-off length (mm)	7, 5
Force in burn-off (kN)	30, 50
Forging force (kN)	50, 80

Source: Author.

Figure 3.2 - Schematic diagram of (a) substrate, (b) stud geometries and (c) thermocouple and micro-hardness measured locations used in experiments. All dimensions are in mm.

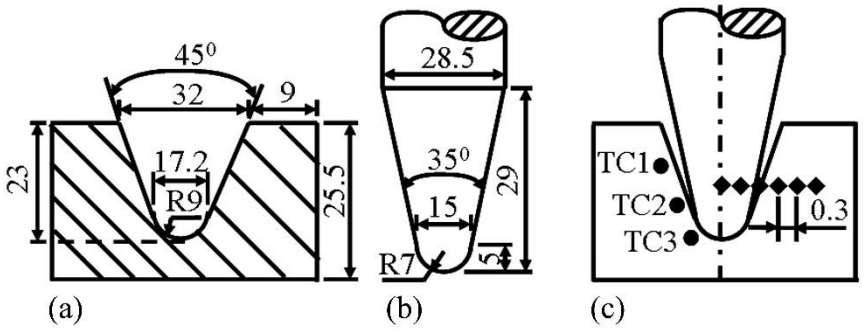

Source: Author.

3.3 THEORETICAL FORMULATION

Figure 3.3 shows the solution domain considered for the modeling including the stud, the pre-machined hole and substrate. A symmetric analysis was carried out considering the axis of stud and pre-machined hole as the axis of symmetry. Figure 3.3 indicates the shape of the stud and substrate hole as a frustum of an inverted cone. A transient heat transfer analysis was conducted considering the governing equation in two-dimensional cylindrical co-ordinate system as

$$\frac{1}{r}\frac{\partial}{\partial r}\left(kr\frac{\partial T}{\partial r}\right)+\frac{\partial}{\partial z}\left(k\frac{\partial T}{\partial z}\right)+\dot{Q}=\rho C_p\frac{\partial T}{\partial t} \tag{3.1}$$

where k, ρ, C_p T and t referred to the thermal conductivity, density, specific heat, and temperature and time variable, respectively. The term $\dot{Q}$ accounts for the rate of heat generation along the stud-hole interface as

$$\dot{Q}=\eta_h[\eta_m(1-\delta)\tau_y+\delta\mu_f P_N](\omega r_1)(A_i/V_i) \tag{3.2}$$

where η_h depicts the fraction of total heat transferred to stud, η_m is the fractional mechanical work due to sticking friction converted to heat, and r_1, ω, P_N and τ_y refer to the radial distance of a point from the stud axis, angular speed of stud, axial pressure on the stud and temperature dependent shear yield stress of stud material,

respectively. The value of η_h was considered as 0.5 that depicted equal partitioning of the heat generated along the stud-substrate interface to both the stud and the substrate as they were of the same material (NANDAN *et al.*, 2007). The value of η_m was considered as 0.4 since that provided the best match between the computed and the measured values of thermal cycles for all cases. The terms A_i and V_i refer to the contact area and volume of an element associated with the interface.

Table 3.3 - Material properties used for ASTM A36 carbon steel in the numerical model.

Thermal conductivity ($Wm^{-1}K^{-1}$)	$63-0.03T$ for T < 1073 K $27[1+(T-1073)/(1175-1073)]$ for T ≥ 1073 K
Specific heat ($Jkg^{-1}K^{-1}$)	$347.3+62.3\exp(T/471.7)$ for T < 1075 K 962.3 for T ≥ 1075 K
Yield strength (MPa)	$190.12-0.1503T$ for T<1500 K; 10 for T ≥ 1500 K

Source: DE; BHADESHIA; DEBROY, (2014) and ROTHMAN (1989).

The local variations in fractional sliding (δ) and coefficient of friction (μf) were considered as

$$\delta = -0.026 + 0.275\exp(r_1\omega/1.87); \quad \mu_f = 0.5\exp(-\delta\, r_1\omega) \tag{3.3, 3.4}$$

following similar expressions used in the modeling of friction stir welding process(NANDAN *et al.*, 2007). Table 3.3 shows the temperature dependent properties of ASTM-A36 steel that are used in the model calculations (DE; BHADESHIA; DEBROY, 2014; ROTHMAN, 1989).

The boundary conditions considered for the modeling are presented schematically in Figure 3.3 and can be expressed as

$$k\frac{\partial T}{\partial n} + h = 0 \tag{3.5}$$

where *h* refers to the convective heat transfer coefficient. Since the maximum temperature in FHPP does not exceed the melting temperature of the alloys, the heat loss due to radiation is neglected. A lumped expression is used to estimate the convective heat loss from the surfaces as

$$h = h_b \times (T - T_0)^{0.25} \tag{3.6}$$

where $h_b = 60\ W\ m^{-2}\ K^{-1.25}$.

The initial contact between the stud and hole was estimated following the equilibrium of force at the stud-hole interface as (DE, 2002)

$$F = \pi r_C^2 \sigma_y \; ; \quad r_C \leq r_{SB} \tag{3.7}$$

where *F* was the applied stud force in burn-off stage, r_C was the average radius of the stud-hole interface and r_{SB} was the radius of the hole at its base. The burn-off stage was divided into a number of small and uniform time-steps. In each time-step, the rate of frictional heat generation was estimated along the stud and hole interface up to the height of the hole filled by plasticized stud material. A detailed discussion of the scheme followed here is presented in APPENDIX 3A. The hardness was estimated based on an analytical scheme available in open literature (ION; EASTERLING; ASHBY, 1984) that used the computed temperature history such as cooling rate and cooling time from 1073 to 773 K from the numerical model. The adopted algorithm for hardness estimation is explained in APPENDIX 3B.

Figure 3.3 - Schematic diagram showing solution domain considered for numerical model with appropriate boundary conditions.

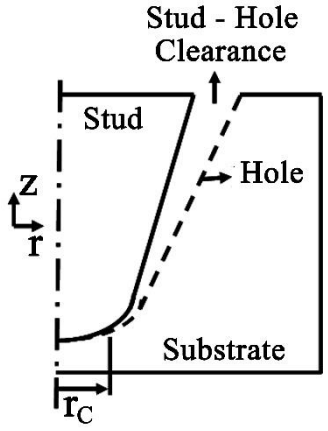

Source: Author.

3.4 RESULTS AND DISCUSSION

Figure 3.4 shows the joint macrographs at three different process conditions. Figure 3.4(a) exhibits a distinct boundary between the stud and the pre-machined crack-hole. The plastic deformation of the stud towards the base of the crack-hole is apparent in Figure 3.4. During the burn-off stage, plasticized stud material fills through the stud-hole clearance with the excess coming out of the hole that is referred to as

flash. A comparison of Figure 3.4(a) and (b) shows an increase in the flash volume as the burn-off length of the stud is increased from 5 to 7 mm. A comparison of Figure 3.4(a) and (c) exhibits a more uniform plastic deformation and joint structure with increase in the stud force from 30 to 50 kN for a constant burn-off length of 5 mm. The blind holes in Figure 3.4 were used to embed thermocouples for temperature measurement during the FHPP.

Figure 3.4 - Joint macrographs corresponding to three different FHPP conditions of stud force (kN) during burn-off stage and stud burn-off length (mm) of (a) (30, 5), (b) (30, 7), and (c) (50,5).

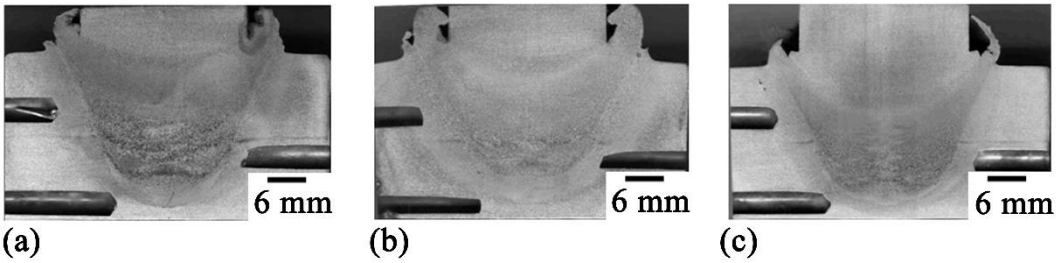

Source: Author.

Figure 3.5 depicts the computed temperature distribution at three different time instants during FHPP of ASTM A36 carbon steel plates for a stud force of 50 kN. The black dashed lines in Figure 3.5 exhibit the original stud and hole boundaries. In Figure 3.5(a) and (b), the white region depicts the stud-hole clearance yet to be filled. A comparison of Figure 3.5(a) to (c) shows that the maximum temperature region moves along with the filling of the stud-hole clearance. This was attributed to the frictional heat generation around the stud and the adjacent plasticized material moving through and filling the stud-hole clearance. The computed peak temperature was 1414 K that was around 80% of the solidus temperature of ASTM A36 steel. The maximum temperature occurred towards the end of the burn-off stage as the relative speed of the material in the stud-hole clearance moved up resulting in increase in relative speed (r_1 in eq. 3.2) and rate of frictional heat generation.

Figure 3.5 - Computed thermal profiles at time instants (a) 2 s, (b) 11 s, and (c) 16 s during FHPP of ASTM A36 carbon steel for a stud force of 50 kN in burn-off stage and burn-off length of 5 mm. All dimensions in the figure are in mm.

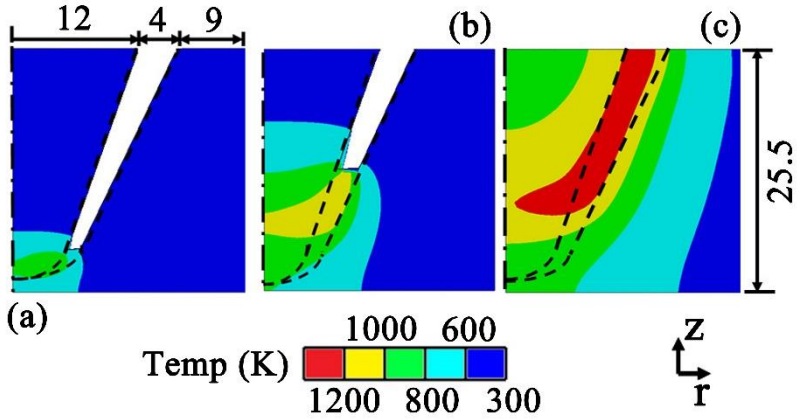

Source: Author.

Figure 3.6(a) and (b) show the computed temperature profile during FHPP of ASTM A36 steel plates for stud forces of 30 and 50 kN, respectively at the end of their respective processing times. The processing time was smaller at a higher stud force. A comparison of Figure 3.6(a) and (b) depicted a decrease in the high temperature region as the stud force was increased. The computed peak temperature exhibited a drop from 1596 to 1570 K as the stud force was increased and the processing time reduced for a constant burn-off length of the stud. Similar range of peak temperature was also reported by Unfried et al. (2010) in FHPP of C-Mn steels.

Figure 3.6 - Computed thermal profiles during FHPP of ASTM A36 carbon steel at stud force (kN) and processing time (s) of (a) (30, 32) and (b) (50, 17) for a constant stud burn-off length of 7 mm. All dimensions in the figure are in mm.

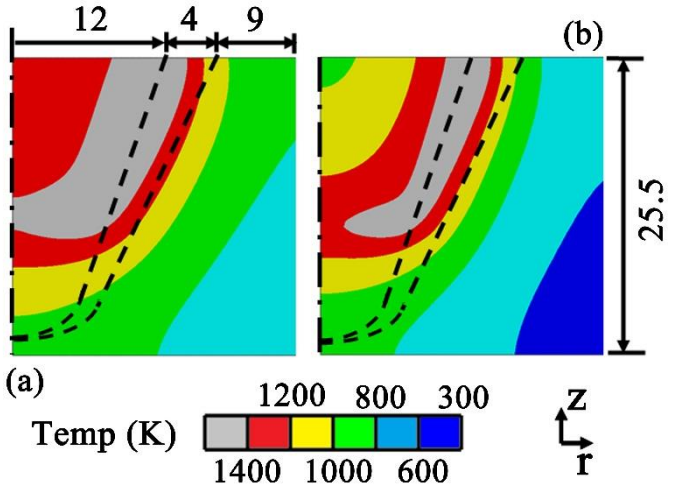

Source: Author.

Figure 3.7(a) and (b) present the computed and the corresponding experimentally measured thermal cycles at two different monitoring locations for two FHPP conditions. Three trials were conducted for each processing condition. The maximum difference in the peak temperature at the measured locations was around 24 K and the error was less than 3%. As the stud deforms and the consolidation of plasticized and sheared material moves up, the rate of heat generation towards the bottom of the hole tends to reduce. As a result, the peak temperature at TC1 has been higher compared to that at TC3, which is closer to the bottom of the pre-machined hole. As the stud rotation is stopped at the end of the burn-off period, the thermal cycles at both the thermocouple locations show a natural cooling trend.

Figure 3.7 also depicted a reduction in the peak temperature with decrease in processing time from 32 to 17 s, and corresponding increase in stud force from 30 to 50 kN. The slight underestimation of peak temperature in both the cases is attributed to the neglect of rate of heat generation due to plastic deformation. Overall, Figure 3.7 shows a fair agreement between the numerically computed and corresponding experimentally measured thermal cycles for two different FHPP conditions.

Figure 3.7 - Computed and corresponding measured thermal cycles during FHPP of ASTM A36 carbon steel at stud force (kN) and processing time (s) of (a) (30, 32) and (b) (50, 17) for a stud burn-off length of 7 mm.

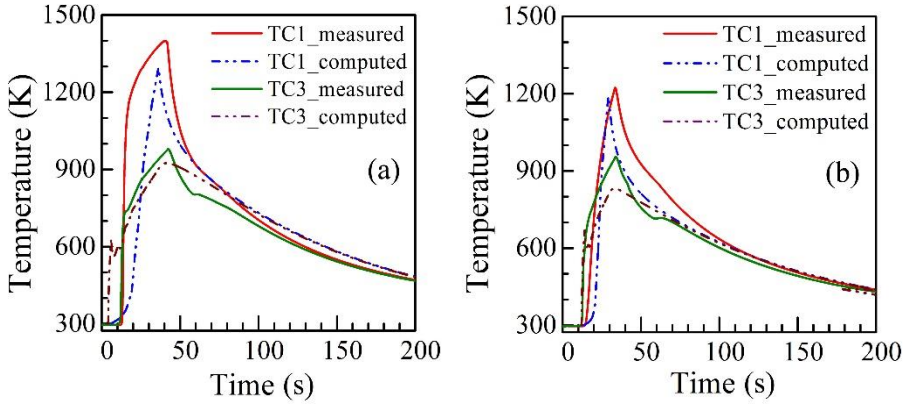

Source: Author.

Figure 3.8(a) and (b) show the measured and corresponding estimated hardness results for two different FHPP conditions. The measured hardness gradually increased towards the joint interface followed by a relatively sharp fall towards the unaffected substrate base material. The range of measured hardness through the plasticized stud material varied approximately from 165 to 210 HV respectively for the

range of process conditions considered here. Similar trend is also reported in literature in FHPP of X65 steel (YIN* *et al.*, 2015; YIN *et al.*, 2015). In friction stir welding of S12 steel, which is similar composition as that of ASTM A36 steel, the measured hardness distribution in the stir zone were also found in the above range (FUJII *et al.*, 2006). The estimated hardness values are in fair agreement with the corresponding measured results although are over-predicted slightly near the stud center. Since the stud is continuously consumed in burn-off stage to fill the clearance, fresh stud material, less affected by the thermal cycle, is continuously being placed in the center (YIN* *et al.*, 2015; YIN *et al.*, 2015). In contrast, the stud is assumed to be fixed in the numerical model, thus creating this difference.

In summary, an axi-symmetric transient heat conduction model was used to compute temperature field and thermal cycles in FHPP of ASTM A36 steel. A novel analytical approach was proposed to account for filling of stud-hole clearance as the stud would be introduced into the crack-hole during FHPP. The processing time was found to be sensitive to the stud force and burn-off length while the peak temperature was more sensitive to the processing time. The highest peak temperature of 1596 K was observed for the bonding made at the lowest stud force of 30 kN and highest burn-off length of 7 mm. The lowest peak temperature of 1414 K was observed for the welding made at highest stud force of 50 kN and lowest stud burn-off length of 5 mm. The hardness values did not vary significantly within the range of process conditions considered. The computed values of thermal cycles and hardness were validated for the range of process conditions considered here.

Figure 3.8 - Estimated and corresponding measured microhardness distribution along the joint transverse sections for stud force (kN) and burn-off length (mm) of (a) (50,7) and (b) (30,5). I, II and III represent stud, clearance and substrate material zones, respectively.

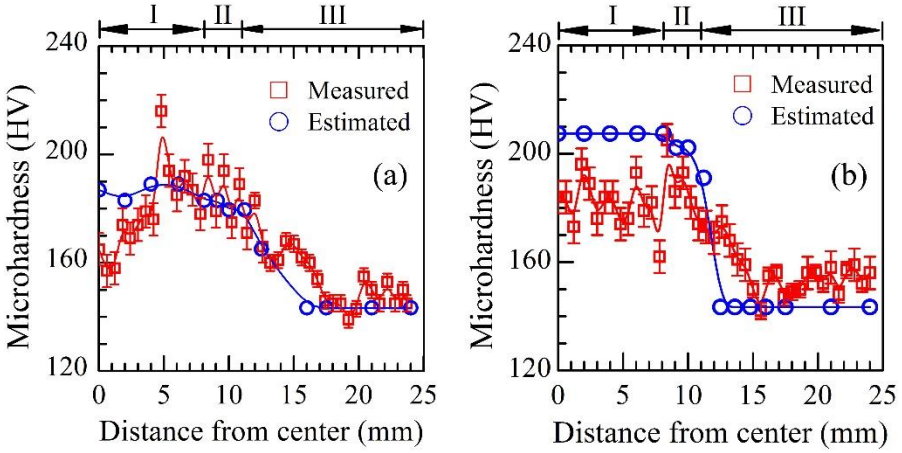

Source: Author.

3.5 CONCLUSIONS

An integrated and simple approach is presented here to compute temperature field and estimate hardness distribution in repairing vis-à-vis filling of crack - holes in thick-walled structure by an external stud using friction hydro pillar processing (FHPP). A larger processing time could lower the requisite stud force but resulted in higher peak temperature and more gentle temperature gradient. As a result, the hardness distribution was found to be more uniform at relatively lower stud force and greater processing time. The estimated thermal cycles and hardness distribution were found to be fairly reliable in comparison to the corresponding experimentally measured results for a wide range of FHPP conditions in ASTM A36 steel.

APPENDIX 3A

The total stud burn-off (L) into the crack-hole is incremented uniformly as H_N in a set of small, discrete time-steps as indicated in Figure 3.9. Considering the stud and substrate as inverted frustums, the stud volume (V_N) undergoing incremental displacements (H_N) is estimated as

$$V_N = \frac{\pi}{3} H_N (r_{ND}^2 + r_{ND} r_{N+1} + r_{N+1}^2) \qquad (3A.1)$$

where r_{ND} and r_{N+1} are the radii at its base and at a height H_N from its base, respectively, of the frustum shape stud with an included angle θ and, $r_{N+1} = r_{ND} + H_N \tan(\theta/2)$. For an incremental advancement of H_N of the stud, the filled-up volume in the stud-hole clearance is estimated as

$$V_{NC} = \frac{\pi}{3} H_{NC} \{(r_{NS}^2 + r_{NS} r_{NS+1} + r_{NS+1}^2) - (r_{ND}^2 + r_{ND} r_{ND+1} + r_{ND+1}^2)\} \qquad (3A.2)$$

where H_{NC} is the height moved by the plasticized material through the stud-hole clearance, and r_{NS+1} and r_{ND+1} are the radii of the hole and stud, respectively, at height H_{NC}, and estimated as $r_{NS+1} = r_{NS} + H_{NC} \tan(\phi/2)$, and $r_{ND+1} = r_{ND} + H_{NC} \tan(\theta/2)$. The term ϕ indicates the included angle of the frustum shape crack-hole. Considering $V_N = V_{NC}$ and substituting r_{NS+1} and r_{ND+1} respectively in terms of r_{NS} and r_{ND}, the value of H_{NC}, r_{NS+1} and r_{ND+1} for a given time-step N are estimated.

Figure 3.9 - Schematic drawing for depiction of the adopted scheme to account for the filling of stud-hole clearance by plasticized stud material.

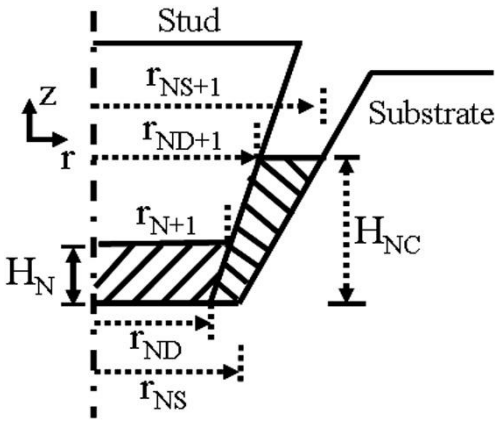

Source: Author.

APPENDIX 3B

The hardness prediction algorithm starts with the calculation of cooling times to form 50% martensite (Δt^M) or 50% bainite (Δt^B) as $\Delta t^M = 10^{(8.79 C_{EQ} - 1.52)}$ or $\Delta t^B = 10^{(8.84 C_{EQ} - 0.74)}$, respectively, where C_{EQ} is the carbon equivalent recommended by the *International Institute of Welding*. The maximum volume fraction that suffers microstructure change (V_{MAX}) is estimated as a function of peak temperature (T_P) and carbon content (C) as

$$V_{MAX} = \begin{cases} 0 \text{ if } T_P \le 996\,K \\ \left(\dfrac{T_P - A_1}{A_3 - A_1}\right) + \left(\dfrac{C}{0.83}\right)\left(\dfrac{A_3 - T_P}{A_3 - A_1}\right) \text{ if } 996K < T_P \le 1118\,K \\ 1 \text{ if } T_P > 1118\,K \end{cases} \quad \text{(3B.1)}$$

The martensite (V_M) and bainite (V_B) volume fractions are estimated as

$$V_M = V_{MAX} \exp[-0.69(\Delta t / \Delta t^M)^2] \quad \text{(3B.2)}$$

$$V_B = V_{MAX} \exp[-0.69(\Delta t / \Delta t^B)^2 - V_M] \quad \text{(3B.3)}$$

where Δt refers to the cooling time from 1073 to 773 K. The perlite-ferrite volume (V_{FP}) is calculated as $V_{FF} = 1 - V_M - V_B$. The Vickers hardness of each of martensite (H_M), bainite (H_B) and ferrite-pearlite (H_{FP}) phases are calculated as

$$H_M = 10 + 949C + 27Si + 11Mn + 8Ni + 16Cr + 21\log(CR) \quad \text{(3B.4)}$$

$$H_B = -360 + 185C + 330Si + 153Mn + 65Ni + 144Cr + 191Mo + (89 + 53C - 55Si - 22Mn - 10Ni - 20Cr - 33Mo)\log(CR) \quad \text{(3B.5)}$$

$$H_{FP} = 50 + 223C + 53Si + 30Mn + 12.6Ni + 7Cr + 19Mo + (10 - 19Si + 4Ni + 8Cr + 130V)\log(CR) \quad \text{(3B.6)}$$

where (CR) is the computed cooling rate from 1073 to 773 K. The final hardness (H) is estimated as

$$H = H_M V_M + H_B V_B + H_{FP} V_{FP} \quad \text{(3B.7)}$$

4 FRICTION HYDRO-PILLAR PROCESSING OF A HIGH CARBON STEEL: JOINT STRUCTURE AND PROPERTIES

Luis Fernando Kanan[2], Buchibabu Vicharapu[1], Antanio Bueno[2], Thomas Clarke*[2] and Amitava De[1]

[1]Indian Institute of Technology Bombay, Mumbai, India
[2]Universidade Federal do Rio Grande do Sul (UFRGS), Porto Alegre, Brazil
(*Corresponding author: tclarke@demet.ufrgs.br)

Metallurgical and Materials Transactions B
Volume 49B, April 2018; p. 699-708
https://doi.org/10.1007/s11663-018-1171-5

4.1 ABSTRACT

A coupled experimental and theoretical study is reported here on friction hydro-pillar processing of AISI 4140 steel, which is a novel solid-state joining technique to repair and fill crack holes in thick-walled components by an external stud. The stud is rotated and forced to fill a crack hole by plastic flow. During the process, frictional heating occurs along the interface of the stud and the wall of crack hole leading to thermal softening of the stud that eases its plastic deformation. The effect of the stud force, its rotational speed and the total processing time on the rate of heat generation and resulting transient temperature field is therefore examined to correlate the processing variables with the joint structure and properties in a systematic and quantitative manner, which is currently scarce in the published literature. The results show that a gentler stud force rate and greater processing time can promote proper filling of the crack hole and facilitate a defect-free joint between the stud and original component.

4.2 INTRODUCTION

Friction Hydro-Pillar Processing (FHPP) is a new solid-state joining technology with unique application such as filling of surface and sub-surface cracks in thick-walled vessels of steels (BULBRING et al., 2013). For example, FHPP was recently attempted for the first time to repair cracks in space shuttle external components of

high-strength aluminum alloys (HARTLEY, 2000). FHPP is also considered in repairing surface cracks in steam turbine rotors of a high-strength, high-temperature-resistant steel (grade26NiCr- MoV14-5) (HATTINGH *et al.*, 2016). Alternative methods such as fusion welding processes for in-service repairing of cracks in components of these high-strength steels remained difficult because of their high hardenability and mandatory need of pre-heating and post-weld heat treatment (PWHT) (ASM INTERNATIONAL HANDBOOK COMMITTEE, 1993; DE ALBUQUERQUE *et al.*, 2009). In contrast, initial FHPP trials could achieve joint strengths up to 90% of the base materials in high-strength steel components, especially those used for petrochemical and thermal power plants (BUZZATTI *et al.*, 2015; HATTINGH *et al.*, 2011; MEINHARDT *et al.*, 2017; YIN *et al.*, 2015). In particular, pressurized pipes and vessels of AISI 4140 steel are widely used in the power generation, oil and gas, and petrochemical industries. Initial studies on FHPP of this alloy have showed promising results. The present work is therefore aimed at probing a systematic investigation of FHPP of AISI 4140 steel.

Fusion welding of AISI 4140 steel is usually recommended in annealed condition and with low hydrogen diffusible filler wires of relatively lower strength, e.g., ER70S-2 and ER80S-D2, because of the very high hardenability of AISI 4140 steel(ASM INTERNATIONAL HANDBOOK COMMITTEE, 2008). Careful pre-heating and PWHT procedures must be followed to avoid cold cracking, reduce residual stresses and decrease impairment of HAZ properties in fusion welding of AISI 4140 steel (SILVA et al., 2009). Since FHPP is a solid-state joining process, several of the aforementioned issues can be alleviated. A systematic analysis of FHPP of AISI 4140 is therefore needed but scarce in the literature.

The effect of stud force and stud rotational speed on joint structure and properties was studied briefly in FHPP of AISI 4140 steel(HATTINGH et al., 2011). A combination of high stud rotational speed of 6000 rpm and a low stud force of 10.5 kN provided fair joint properties that were comparable to those of the base materials (HATTINGH et al., 2011). An increase in stud force led to faster plastic flow of the stud and therefore reduced the overall processing time and peak temperature (BULBRING et al., 2013; CHLUDZINSKI et al., 2012). However, the effect of the reduced processing time and lower peak temperature on the joint properties were not well addressed in the literature. Improper selection of the stud force often led to ‘‘lack of filling’’ defects near the crack hole bottom in FHPP of high-strength steels (MEYER,

2003). FHPP is also attempted under water to reduce the peak temperature in components of high-strength line pipe X65 steels (YIN *et al.*, 2015). However, the resulting joint exhibited a full martensite structure due to higher cooling rates (YIN *et al.*, 2015). A fairly uniform hardness distribution across the joint was reported in FHPP of C-Mn steel especially at lower stud forces (VICHARAPU et al., 2017). Although these studies provided an insight into FHPP of steels, a quantitative understanding of the effect of process variables on the temperature field, cooling rate and resulting joint hardness distribution remained scarce in FHPP of high-strength steels.

In FHPP, the real-time monitoring of temperature is challenging because of the continuous plastic deformation of the stud material inside the crack hole (UNFRIED S. et al., 2010). Therefore, numerical modeling of FHPP was considered as a recourse to compute the evolution of the temperature field, thermal cycles and cooling rate in FHPP.

VICHARAPU et al., (2017) showed that the evolution of temperature field, thermal cycles and cooling rate in the joint area could be realized using a numerical heat transfer model in a preliminary study on FHPP of ASTM A36 steels. A coupled experimental and numerical investigation is therefore undertaken on FHPP of AISI 4140 steel. The effect of force rate on the rate of heat generation, thermal softening and plastic deformation of the stud, and the overall processing time was studied in a comprehensive manner. A two-dimensional axi-symmetric transient heat transfer analysis was carried out to compute the temperature distribution and thermal cycles. The computed thermal cycles were tested with the corresponding measured results and used to estimate the hardness distribution in the joint area following available empirical relations. The estimated hardness distributions were also tested with the corresponding measured results.

4.3 EXPERIMENTAL SET-UP AND PROCEDURE

Figure 4.1(a) shows the experimental set-up for FHPP in a schematic manner. The legends F, N and L refer to the stud force and its rotational speed and the length of the stud pushed into the crack hole, respectively. Figure 4.1(b) shows the typical nature of variations of the stud rotational speed and force and its insertion into the crack hole in three consecutive periods that are referred to as the dwell (t1), burn-off (t2) and forging (t3) stages. All the FHPP experiments were conducted using a specially designed force-controlled displacement of the stud at the LAMEF-UFRGS,

Brazil (CHLUDZINSKI *et al.*, 2012). Table 4.1 presents the chemical composition of the stud and substrate materials, both of which are taken as AISI 4140 steel.

Figure 4.1 - (a) Schematic diagram of the FHPP setup and (b) typical responses of stud rotational speed (N), stud force (F) and stud burn-off length (L) in dwell (t1), burn-off (t2) and forging (t3) stages, where t1, t2 and t3 indicate respective time durations.

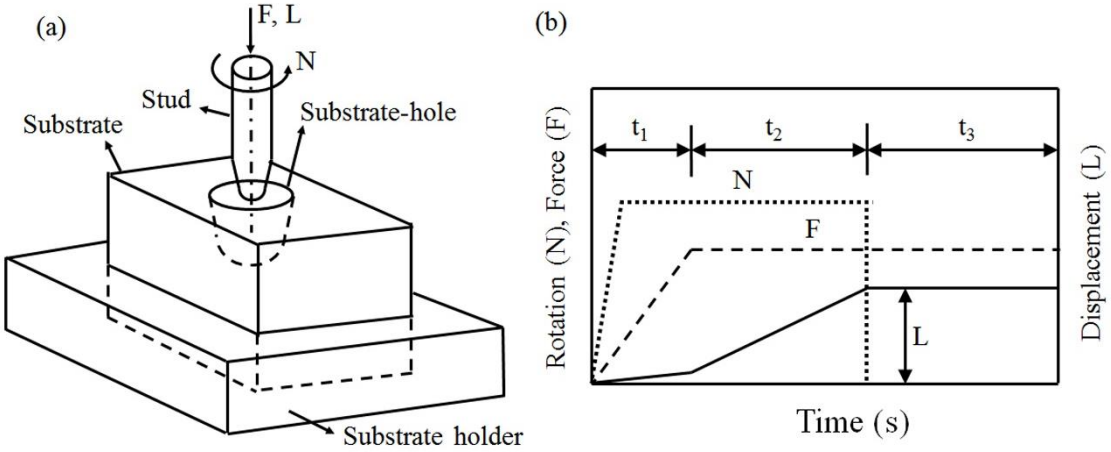

Source: Author.

As indicated in Figure 4.1(b), the stud force rises at a pre-set rate during the dwell stage to a constant value. As a result, heating due to friction occurs along the interface of the stud and base of the crack hole leading to thermal softening and plastic flow of the stud. Part of the plasticized stud is also allowed to come out as a flash to ensure adequate filling of the crack hole, which marks an end of the burn-off period, and the stud rotation is stopped. A constant stud force is still maintained, and often the same is augmented, to facilitate the consolidation of the plasticized material inside the crack hole and form a solid-state joint with the original component in the forging stage. Previous studies showed the presence of typical voids at the root of the crack hole in FHPP of DH36 steel (DE LIMA LESSA *et al.*, 2016) and AISI 4140 steel (HATTINGH *et al.*, 2011). In underwater FHPP of SS235 stainless steel, voids were found near the crack-hole base, which was attributed to inadequate heat generation and insufficient plastic flow of the stud material at the initial period (CUI *et al.*, 2014). In under- water FHPP of X65 line pipe steels, the ‘‘lack of filling’’ defect near the crack-hole base was observed, which was attributed to insufficient stud force (YIN *et al.*, 2015). Therefore, the force rate in dwell stage was considered as one of the main process variables in the present study for the first time in the FHPP literature.

Three different stud force rates were considered in the dwell stage as shown in Table II. The maximum stud length to be forced into the crack hole, referred to as the burn-off length, the stud rotational speed during the dwell and burn-off stages, and the final stud force in the burn-off and forging periods were kept constant at 7 mm, 5000 rpm and 25 kN, respectively (Table 4.2). The dwell time (t1) ends as the final stud force of 25 kN or the maximum burn-off length of 7.0 mm is reached at a given stud force rate. At higher force rates of 4.0 and 8.0 kN/s, the maximum stud burn-off length of 7.0 mm was consumed while a burn-off length of 6.5 mm could be used at the lower force rate of 2.0 kN/s (Table 4.2). The burn-off time (t2) allows further pushing of the stud into the crack hole to ensure adequate filling of the crack hole. However, the burn-off time (t2) is eliminated if the crack hole is already filled with flashes emerging out by the end of the dwell stage (t1). In contrast to dwell (t1) and burn-off (t2) times, the forging time (t3) is a pre-set process variable (VICHARAPU *et al.*, 2017).

Table 4.1 - AISI 4140 steel chemical composition (in wt%).

C	**Cr**	**Mo**	**Si**	**P**	**S**	**Mn**	**Ni**
0.4	0.9	0.2	0.2	0.01	0.01	0.85	< 0.005

Source: Author.

Table 4.2 - Process conditions considered in FHPP of AISI 4140 steel.

Rotational speed (N, rpm)	Burn-off length (L, mm)	Force (F, kN)		Force rate in dwell stage (kN/s)	Processing times (s)		
		Burn-off stage	Forging stage		Dwell stage (t_1)	Burn-off stage (t_2)	Forging stage (t_3)
5000	6.5	25	25	2.0	12.5	0.0	15
	7.0			4.0	6.2	6.5	
	7.0			8.0	3.2	10.5	

Source: Author.

Figures 2(a) and (b) show the stud and crack-hole geometries used for the experiments. Three K-type thermocouples of 1.0 mm diameter were located just outside the crack-hole wall at three different heights from the crack-hole base as shown in Figure 2(c). Each thermocouple was calibrated according to ASTM E230/ E230M (ASTM INTERNATIONAL, 2017) and spot-welded in a pre-drilled hole. The

thermal cycles were measured at a simultaneous sampling rate of 5.0 Hz. Transverse joint sections were polished and etched with Nital solution to view the joint macrographs. Figure 2(c) also shows the locations used to measure Vicker's micro-hardness, which was evaluated using a load of 0.5 kg and holding time of 10 seconds.

Figure 4.2 - Schematic diagrams of (a) stud, (b) substrate with crack-hole, and (c) thermocouple and micro-hardness measurement locations. All dimensions are in mm.

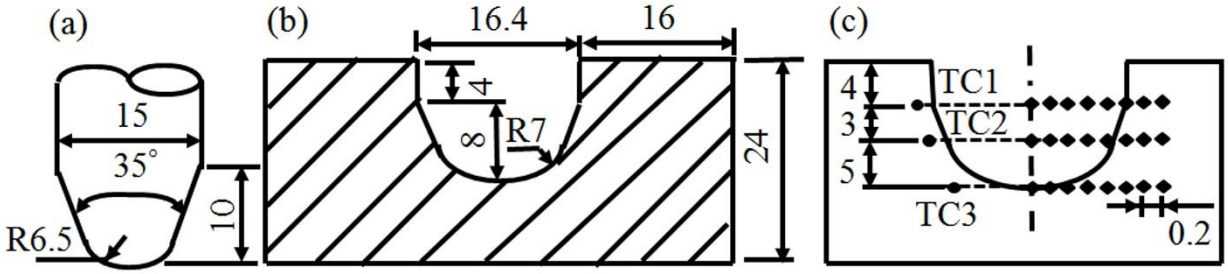

Source: Author.

4.4 THEORETICAL FORMULATION

A transient heat transfer analysis was conducted considering the governing equation in two-dimensional cylindrical co-ordinate system as

$$\frac{1}{r}\frac{\partial}{\partial r}\left(kr\frac{\partial T}{\partial r}\right)+\frac{\partial}{\partial z}\left(k\frac{\partial T}{\partial z}\right)+\dot{Q}=\rho C_p\frac{\partial T}{\partial t} \tag{4.1}$$

where *k, ρ, C_p T* and *t* referred to the thermal conductivity, density, specific heat, and temperature and time variables, respectively. The term $\dot{Q}$ accounts for the rate of heat generation along the interface of the stud and wall of the crack-hole as

$$\dot{Q}=[\eta_m(1-\delta)\tau_y+\delta\mu_f P](r_1\omega)(A_i/V_i) \tag{4.2}$$

where η_m is the fractional mechanical work converted to heat, P the axial pressure on the stud, ω the stud angular speed, r_1 the radial distance of any point from the stud axis and τ_y the temperature dependent shear yield strength of stud material at r_1. The value of η_m was considered as 0.3 based on similar range of values used in modeling of friction stir welding (BUCHIBABU; REDDY; DE, 2017; NANDAN *et al.*, 2007). The terms A_i and V_i refer to the contact area and volume of an element associated with the interface. The terms δ and μ_f refer to the local variations in fractional sliding and co-efficient of friction along the joint interface, and are considered as

$$\delta=-0.026+0.275\exp(r_1\omega/1.87);\quad \mu_f=0.5\exp(-\delta r_1\omega) \tag{4.3, 4.4}$$

following similar expressions used in modeling of friction stir welding (NANDAN *et al.*, 2007) and FHPP of A36 steel (VICHARAPU *et al.*, 2017). A lumped heat transfer coefficient (h) was used to account for the convective heat loss from the surfaces as

$$h = h_b \times (T - T_0)^{0.25} \quad (4.5)$$

where $h_b = 65\ W/m^2 K^{1.25}$.

Figure 4.3(a) shows the solution domain including the stud, crack-hole and the substrate considered for the heat transfer analysis. Figure 4.3(b) and (c) show schematic presentations of the solution domain with the stud - crack-hole clearance filled partially and completely. The filling of the stud - crack-hole clearance by the plasticized material was considered uniformly in an incremental manner through a number of discrete time-steps (VICHARAPU et al., 2017). The hardness distribution across the joint area was estimated as function of cooling rate and hold time between the temperature range of 1073 K (800 ºC) to 773 K (500 ºC) following available analytical relations for alloys of similar compositions (ION; EASTERLING; ASHBY, 1984). The empirical relations used for hardness calculations are presented in Appendix-A. The cooling rate and hold time between the specified temperature ranges were obtained from the numerically computed results. The model calculations considered temperature dependent material properties (Table 4.3).

Table 4.3 - Thermo-physical properties of AISI 4140 steel

Density (kg/m^3)	7830
Solidus temperature (K)	1750
Thermal conductivity (W/mK)	$54.91-3.33e^{-2}\times T+1.0e^{-5}\times T^2$ for $T < 1200$ K 30.0 for $T \geq 1200$ K
Specific heat (J/kgK)	$361.55 + 1.13e^{-1}+3.0e^{-4}\times T^2$ 300 K ≤ T ≤ 1200 K 607.0 for T > 1200 K
Yield strength (MPa)	$919.61-1.21\times T+4.21e^{-4}\times T^2$ for T ≤ 1200 K 13.0 for T > 1200 K

Source: LAKHKAR; SHIN; KRANE (2008)

Figure 4.3 - a) Schematic diagram of the solution domain considered for the numerical model. Computed results are shown for the dotted portion in zoomed view. Schematic diagrams (b) and (c) respectively show partially filled and fully filled stud-crack-hole clearance.

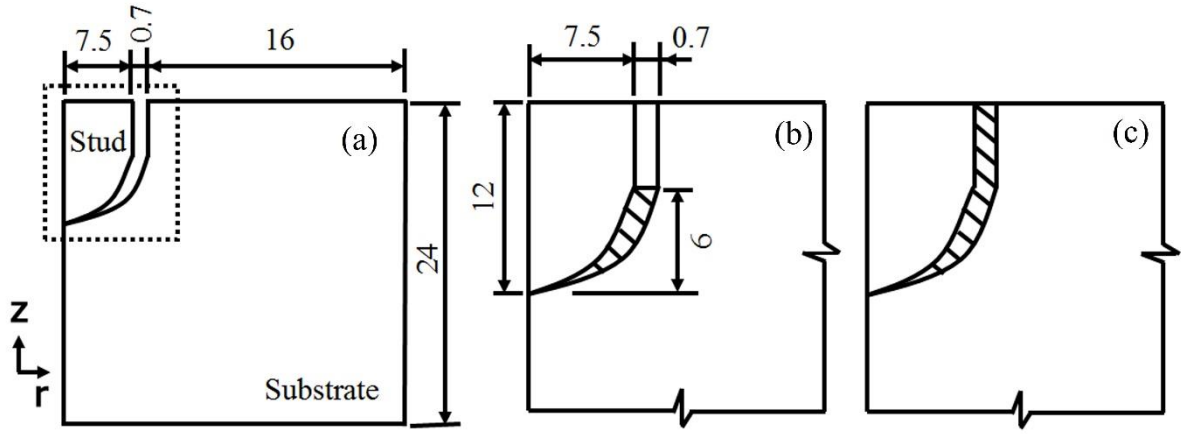

Source: Author.

4.5 RESULTS AND DISCUSSION

Figure 4.4 shows the FHPP joint macrographs at three different force rates with the dashed lines highlighting the original crack-hole boundary. The black slots, three in each case, with taper ends were used to fix the thermocouples for measurement of thermal cycles. In each case, the crack-hole is completely filled by plastically deformed stud material as noted in Figure 4.4(a-c). At a force rate of 2.0 kN/s, the joint was free of any void or lack of filling as indicated in Figure 4.4(a). In contrast, a small crack-like defect is noted near the bottom of the crack-hole for the FHPP joint made at the force rate of 4.0 kN/s as shown in Figure 4.4(b). The zoomed view of the defect region is shown in Figure 4.4(d) although the same does not exhibit a large void or network of small cracks.

Figure 4.4 - Macrographs of the joints at different force rates (kN/s) of (a) 2.0, (b) 4.0, and (c) 8.0. Regions highlighted in red color in macrographs (b) and (c) show defects in the processed zone. Images (d) and (e) are the magnified views of defects in (c).

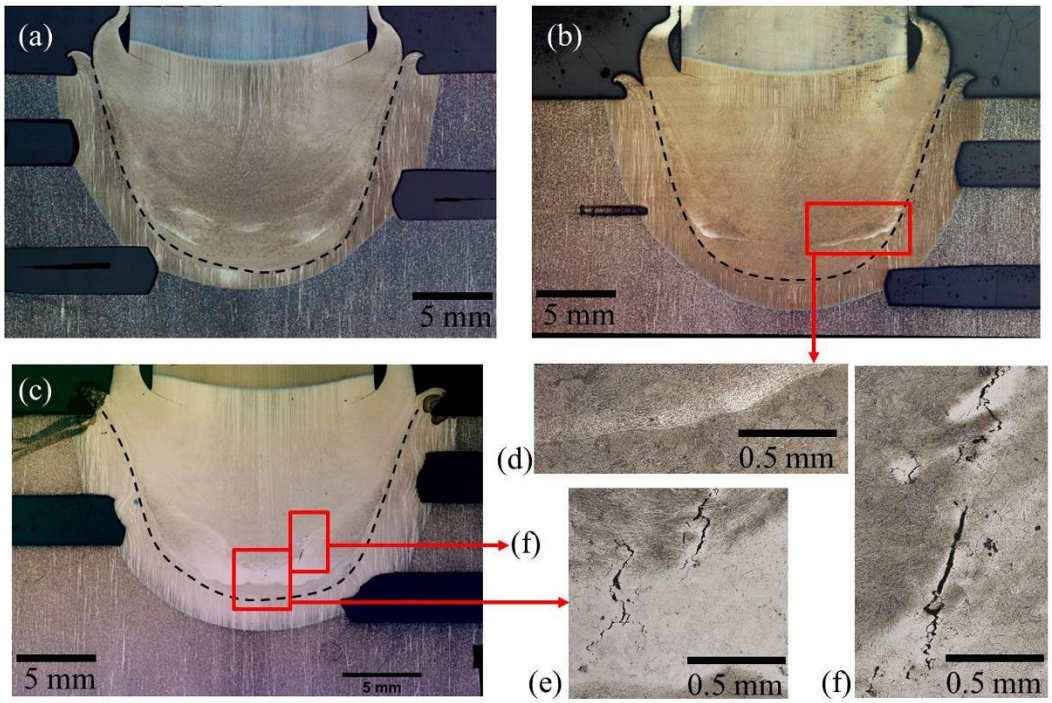

Source: Author.

Figure 4.4(c) shows the FHPP joint at the highest force rate of 8.0 kN/s with several small discontinuities near the base of the crack-hole as indicated by two red color boxes. The zoomed views of these two defect regions are shown in Figure 4.4(e-f) that exhibit network of discontinuities in the processed zone. Rise in force rate promotes a faster insertion of the stud inside the crack-hole at a shorter dwell period resulting in inadequate thermal softening and localized discontinuities. Similar defects were reported by MEYER (2003) and CUI *et al.* (2014) in FHPP of X65 and S355 steels, respectively. Overall, the joints prepared at the force rate of 2.0 kN/s exhibited defect free joint.

Figure 4.5(a-c) show the computed temperature isotherms at three different force rates of 2.0 kN/s, 4.0 kN/s, and 8.0 kN/s, respectively at a time instant of 3.2 s that confirms to the end of dwell stage at the force rate of 8.0 kN/s (Table 4.2). The two white dashed lines in Figure 4.5 depict the original stud boundary and the wall of the crack-hole, and thus the region enclosed between these two lines depicts the original clearance to be filled-up by deformed stud material. Figure 4.5(a) shows that at the force-rate of 2.0 kN/s, the clearance between the stud and the crack-hole is not

yet filled up at the end of 3.2 s. In contrast, the crack-hole is completely filled up at the other two force rates of 4.0 kN/s and 8.0 kN/s as depicted in Figure 4.5(b-c). A comparison of Figure 4.5(a-c) shows that the maximum temperature towards the base of the crack-hole tends to reduce with increase in force rate at the time instant of 3.2 s. This was attributed to rapid introduction and deformation of the stud at higher force rates that allowed lesser time for frictional heating. In contrast, lower force rate allowed adequate time to frictional heating and ease of plastic deformation of stud material along the interface of stud and base of crack-hole.

Figure 4.5 - Computed isotherms at time instant of 3.9 s at stud force rate (kN/s) of (a) 2.0, (b) 4.0, and (c) 8.0 during FHPP of AISI 4140 steel.

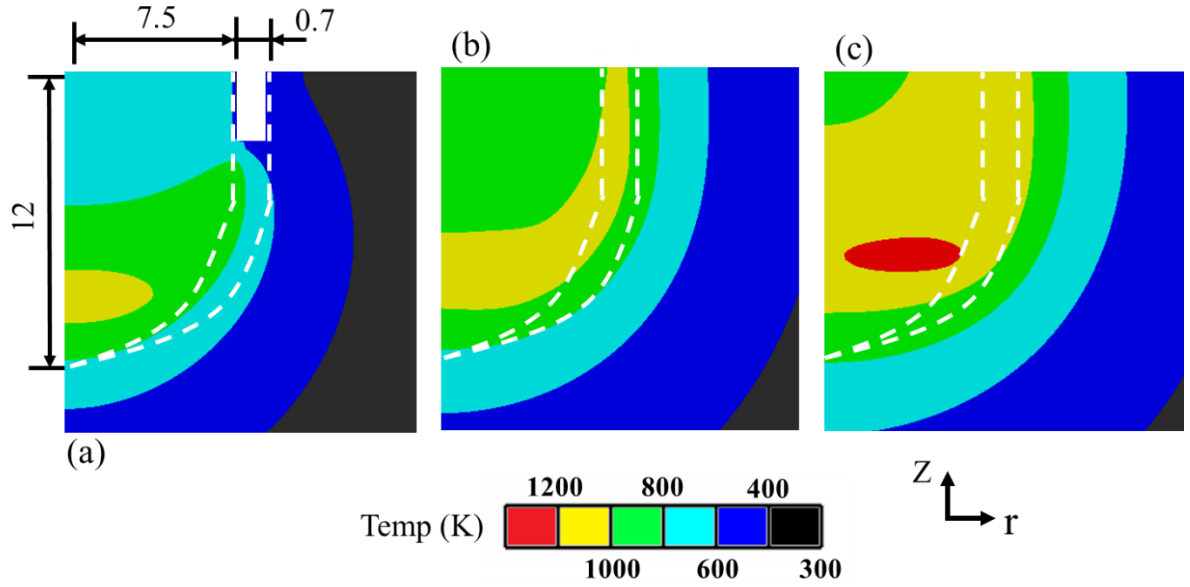

Source: Author.

Figure 4.6(a-c) show the computed temperature isotherms at the time instant of 12.5 s that corresponds to the end of dwell stage at the lowest force rate of 2.0 kN/s. Figure 4.6(a) shows that the crack-hole is filled up even at the lowest force rate of 2.0 kN/s. Further, almost the complete stud exhibited the maximum temperature of 1200 K for all the force-rates. At the lowest force rate of 2.0 kN/s, the stud force reached to the maximum value of 25 kN at the end of 12.5 s while at higher force rates of 4.0 kN/s and 8.0 kN/s, the maximum force was attained earlier as 6.5 s and 3.2 s, respectively (Table 4.2). As a result, the hotter region of the stud widened with rise in force rates.

Figure 4.6 - Computed isotherms at time instant of 12.1 s at stud force rate (kN/s) of (a) 2.0, (b) 4.0, and (c) 8.0 during FHPP of AISI 4140 steel.

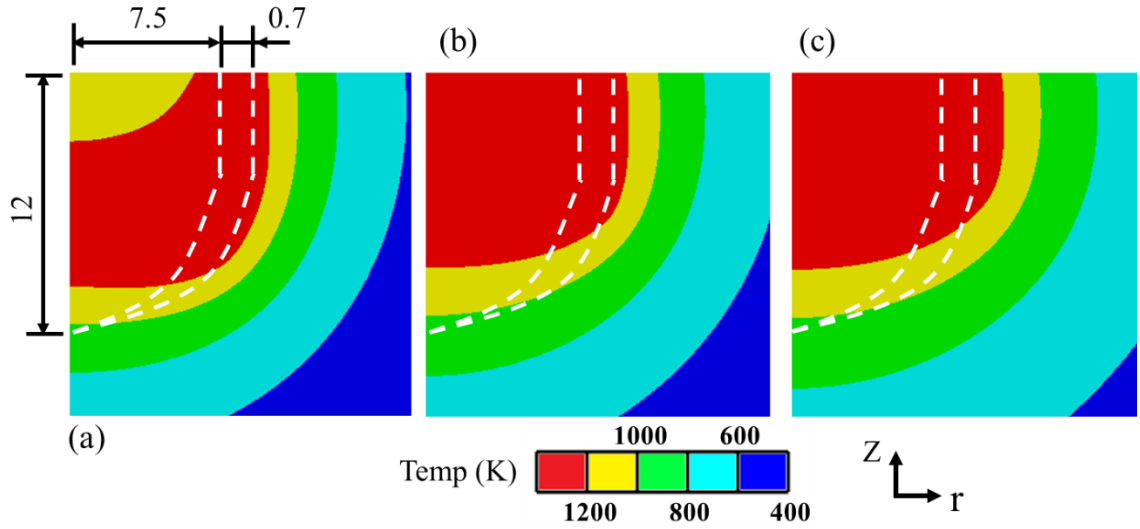

Source: Author.

Quantitative knowledge of the thermal cycles and cooling rate is considered requisite to assess the structure and properties of the joint region in FHPP. Figure 4.7(a-c) show the computed thermal cycles at three different locations, which are considered within the stud and at three different heights from the crack-hole base. Figure 4.7(a) shows that the thermal cycles at the location very near to the crack-hole base. The thermal cycles in Figure 4.7(a) depict a rapid rise to a peak followed by a gentle cooling up to a certain time and then, faster cooling. The initial rise in temperature is due to the heat generation due to friction along the interface of stud and crack-hole base. As the plasticized stud material deforms and piles up through the stud - crack-hole clearance, heat dissipation through the bulk material increases leading to gradual cooling of the joint region near to the crack-hole base. At the end of dwell and burn-off stages, the stud rotation stops leading to no further heat generation and the interface cools down faster. Figure 4.7(a) implies slightly higher peak temperature at the lowest force-rate of 2 kN/s that is attributed to slower rate of introduction of the stud and consequent delayed filling of the stud - crack-hole clearance volume by plasticized stud material.

Figure 4.7(b) shows the computed thermal cycles at a height of 3 mm from the crack-hole base for all the three force-rates. The peak temperature in each case is higher and also, attained at later time instants in comparison to that in Figure 4.7(a) as the filling of stud - crack-hole clearance occurs gradually from the bottom. Figure

4.7(b) also shows that the peak temperatures reach after a certain time instant that nearly correspond to the time to fill the height of 3 mm along the stud - crack-hole clearance zone at different force rates. The faster cooling in Figure 4.7(b) corresponds to the end of the dwell and burn-off stages when the stud rotation and thus, frictional heat generation stops. The computed thermal cycles in Figure 4.7(c) are at a height of 6 mm from the crack-hole base and attained further delayed and higher peak temperature. Thus, the computed thermal cycles in Figure 4.7(a-c) could embody the effects of frictional heat generation, filling of stud - crack-hole clearance by plasticized material, heat dissipation through the bulk material, and subsequent cooling as they occurred in different locations of the joint region during FHPP.

Figure 4.7 - Computed thermal cycles at different stud radii (mm) and heights (mm) from the base of the crack-hole as (a) (2.0, 0.0), (b) (3.0, 3.0), and (c) (3.7, 6.0).

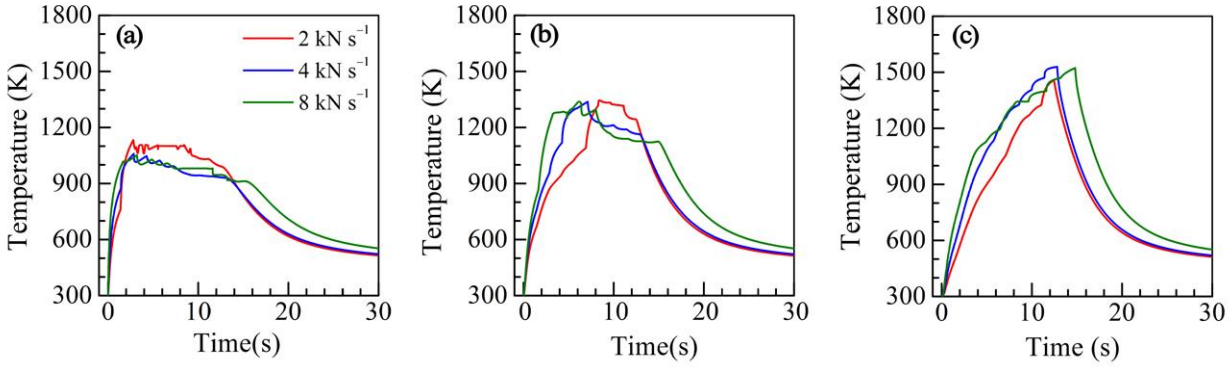

Source: Author.

Figure 4.8(a-c) show the computed and the corresponding measured thermal cycles at two different thermocouple monitoring locations, TC1 and TC2 (Figure 4.2c). The measured peak temperatures increased steadily with rise in stud force rates, as was expected. As a result, the measured cooling rates at TC1 increased from 41.66 K/s to 57.69 K/s and, at TC2 from 35.36 K/s to 46.15 K/s with rise in force rates from 2.0 kN/s to 8.0 kN/s. The computed peak temperatures and cooling rates were within 4.6 % error with the corresponding measured results at the lowest stud force rate of 2.0 kN/s (Figure 4.8a). At the highest force rate of 8.0 kN/s, the computed peak temperatures and cooling rates were under-predicted by around 18 % that was attributed to the neglect of heating due to plastic deformation of stud material. The range of the peak temperatures and cooling rates suggest a martensitic phase formation for AISI 4140 steel (ASM INTERNATIONAL HANDBOOK COMMITTEE,

2008). A higher hardness of the processed zone was thus expected compared to that in the unaffected substrate material.

Figure 4.8 - Computed and corresponding measured thermal at selected thermocouple locations TC1 and TC3 of during FHPP of AISI 4140 steel at stud force rate (kN/s) of (a) 2.0 and (b) 4.0 and (c) 8.0.

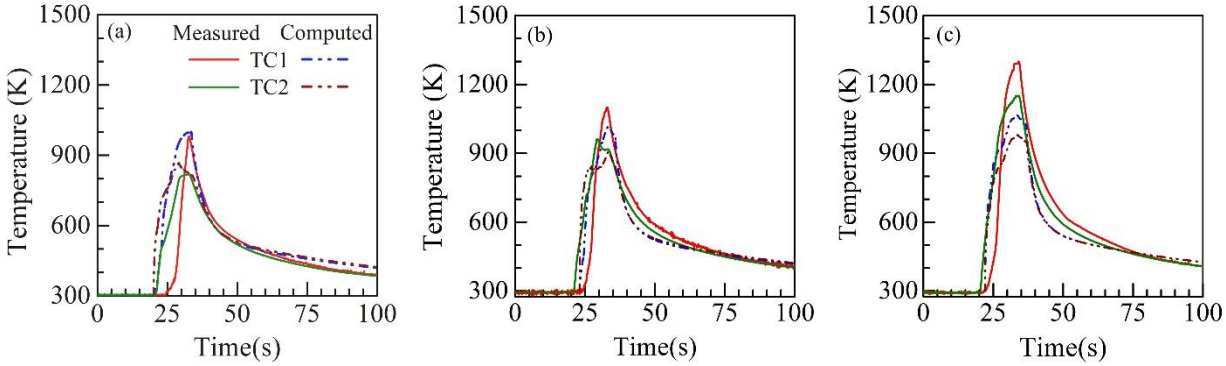

Source: Author.

Figure 4.9(a-c) show the estimated and the corresponding measured hardness results at a height of 8.0 mm from the base of the crack-hole at three different force rates of 2 kN/s, 4 kN/s and 8.0 kN/s, respectively. The hardness values remained high around 650 HV and uniform for the complete joint region up to the original crack-hole wall and depicted a sharp drop afterwards. The width of the region with higher hardness increased at greater stud force rates as higher forces resulted a wider region with high peak temperature as shown in Figure 4.6. The high hardness in the processed joint region was attributed to the formation of harder phases such as martensite due to high hardenability of AISI 4140 and steep cooling rate. Figure 9(a) exhibits traces of localized high-hardness spikes in the stud-substrate clearance region, which is filled by the stud material at high strain rates and temperature during FHPP. As the FHPP joint is not tempered afterwards, such hardness variations in regions of high deformation and temperature gradient are perhaps expected.

Figure 4.10 and Figure 4.11 show the computed and the corresponding measured hardness values across the processed joint region at typical heights of 5.0 mm and along the base of the crack-hole base, respectively. The nature of variations of the hardness distribution across the joint regions in Figure 4.10 was nearly the same with that noted in Figure 4.9 except that the width of the high hardness regions were slightly smaller in Figure 4.10. This was attributed to the reduced peak temperature and cooling rate experienced at a lower height of 5.0 mm. Closer to the

crack-hole base, both peak temperatures and cooling rates of the joint region reduced further and as a result, the width of the processed region with higher hardness values decreased further as depicted in Figure 4.11. The experimentally measured hardness values in Figure 11 were consistently higher than the corresponding computed results, attributed to the fine-grained structure of the material and presence of hard martensite phase. However, the effect of grain size was not considered in empirical relations used for the estimation of hardness. A comparison of Figure 4.9, Figure 4.10 and Figure 4.11 show that the maximum width of the high temperature region reduced from around 8.5 mm to 4.0 mm from the top to the bottom for the processing conditions considered here.

Figure 4.9 - Measured vis-à-vis estimated hardness at a height of 8.0 mm above the crack-hole base at stud force rates (kN/s) of (a) 2.0, (b) 4.0, and (c) 8.0.

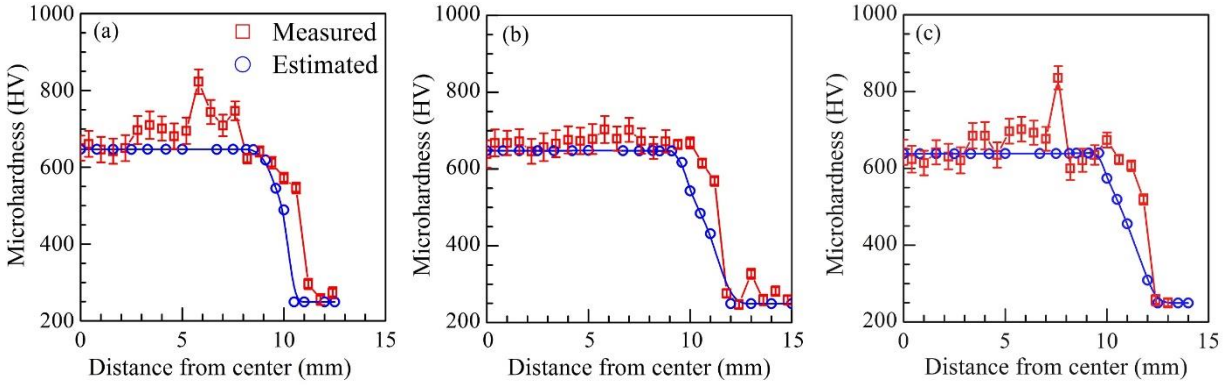

Source: Author.

Figure 4.10 - Measured vis-à-vis estimated hardness at a height of 5.0 mm above the crack-hole base at stud force rates (kN/s) of (a) 2.0, (b) 4.0, and (c) 8.0.

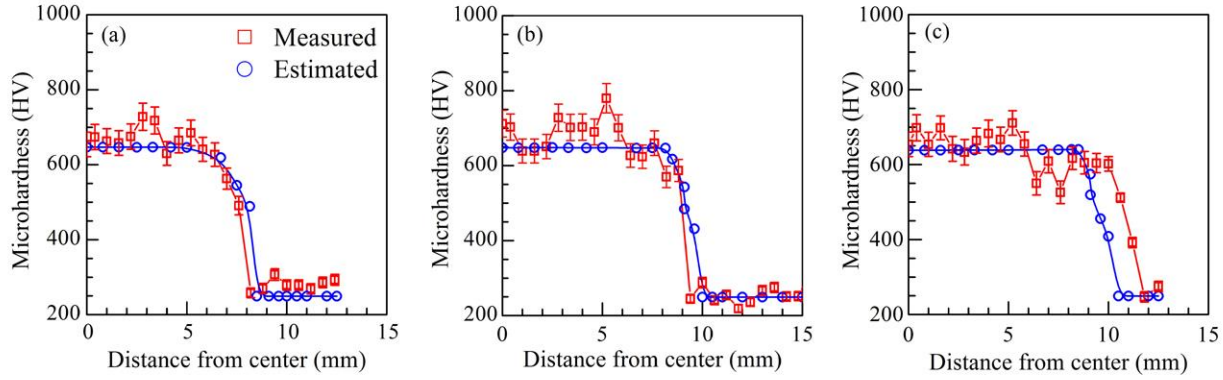

Source: Author.

Figure 4.11 - Measured vis-à-vis estimated hardness along the base of the crack hole at stud force rates (kN/s) of (a) 2.0, (b) 4.0, and (c) 8.0.

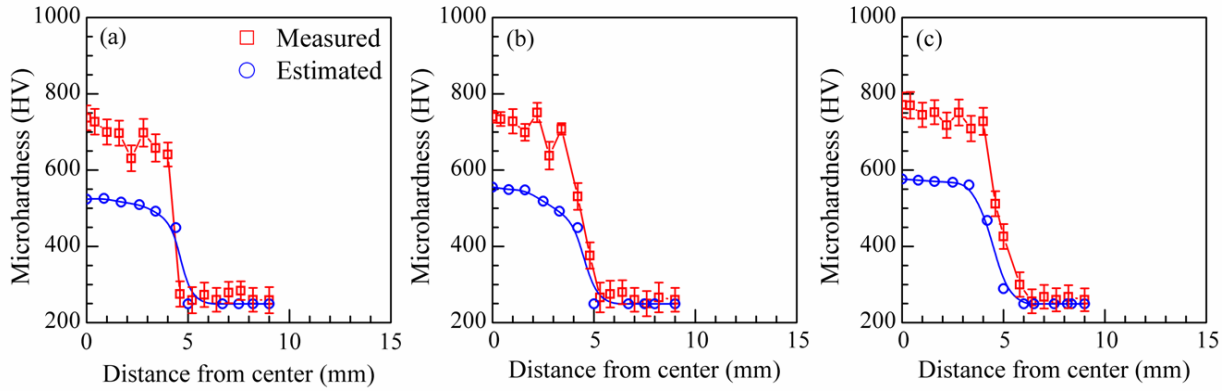

Source: Author.

The measured average hardness values within the processed zone were in the range of 620 HV to 750 HV, and the corresponding computed values were 525 HV to 650 HV. The slight under-prediction in the computed hardness values was attributed to the simplified empirical relations that remained inadequate to realize the competitive nature of solid state phase transformations fully accurately. The numerically computed temperature field and thermal cycles depict the ranges of peak temperature around 1200 to 1500 K and cooling rates around 45 to 130 K/s (between 1073 and 773 K) for the FHPP conditions considered here. Such cooling rate ranges are expected to result in a predominant martensitic structure in the processed zone of AISI 4140 (ASM INTERNATIONAL HANDBOOK COMMITTEE, 1991). Figure 12 shows the FHPP joint at a force rate of 2 kN/s and typical EDS analysis and images from optical microscopy (OM) and scanning electron microscopy (SEM) of a localized region as shown by a red box in Figure 4.12(a). Detailed examination of the results from EDS, OM and SEM analyses did not reveal the presence of a tempered martensitic structure or carbide concentration. In addition, the EDS results showed a homogeneous distribution of Cr, Mo and C with no indication of regions with higher element concentration.

Figure 4.12 - (a) FHPP joint macrograph for the force rate of 2 kN/s and (b) EDS image, (c) optical micrograph and (d) SEM backscattered image of a selected region including stud-substrate joint and the adjacent regions as shown by the red open box in (a).

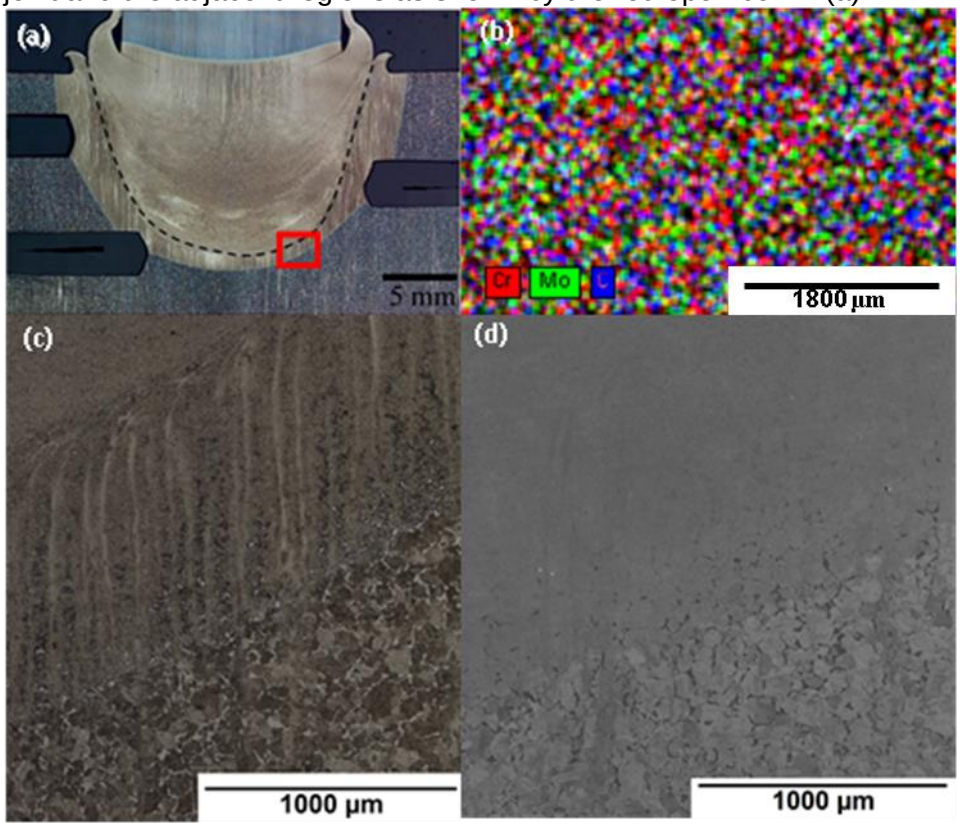

Source: Author.

An attempt is made further to explain the likely formation of a martensitic structure by superimposing the cooling curves [Figure 4.7(c)] on a typical CCT (continuous-cooling-transformation) diagram of AISI 4140 in Figure 4.13 (APPENDIX 4A) (CORDOVILLA *et al.*, 2016). Figure 4.13 confirms that the martensite phase transformation in the processed zone is expected and illustrates the application of the hardness estimation algorithm as presented in APPENDIX 4A. HATTINGH *et al.* (2011) reported a similar range of hardness values in FHPP of AISI 4140 steel, and CORDOVILLA *et al.* (2016) also reported similar values in laser hardening of AISI 4140 steel.

In summary, a coupled experimental and numerical analysis was carried out to study the effect of force rate and other key process variables in FHPP of AISI 4140 steel. An axisymmetric transient heat conduction model was developed to compute temperature field and thermal cycles. Adequate filling of the stud-crack-hole clearance and sound joint structure was obtained at a lower stud force rate of 2.0 kN/s, while the joints showed voids near the crack-hole bottom when FHPP was performed at higher

force rates of 4.0 and 8.0 kN/s. Also, a lower force rate needed greater processing time to fill-up the crack hole, resulting in a smaller joint region with high hardness values. The computed thermal cycles and subsequently estimated hardness values showed fair agreement with the corresponding measured results. The influence of residual stresses was not addressed in the current analysis, but nonetheless should have an important effect on component usage, since thermal and mechanical stresses are abundant. Further studies are in progress to measure and predict the profile and magnitude of residual stresses through the weld with the objective of creating a useful tool to assess the appliance of FHPP in steels.

4.6 CONCLUSIONS

The present study aimed to eliminate the most commonly reported voids and crack-like defects near the crack-hole base in friction hydro pillar processing of steels. Force rate was considered as one of the main input process variables in FHPP for the first time in literature. Higher force rates decrease the processing time during dwell stage and increases the formation of crack like defects in the bottom situ of the filled substrate hole due to inadequate thermal softening and localized discontinuities. A gentler increase in contact force with time during dwell stage is then envisaged as the proper solution. All tested conditions presented martensite formation in the processed zone and a transient heat transfer model could be able to simulate the thermal profiles and estimate material hardness with reasonable accuracy. This thoroughly validated heat transfer model can be further used for an estimation of temperature distribution, joint structure and properties.

APPENDIX 4A

The hardness distribution across the joint is estimated using the numerically computed cooling rate and holding time between 1073 K and 773 K at any given location and analytical-cum-empirical relations for prediction solid-state phase transformations and consequent hardness for steels of similar compositions available in published literature (ION; EASTERLING; ASHBY, 1984). The cooling times to form either 50% martensite (Δt_M) or 50% bainite (Δt_B) is estimated as

$$\Delta t_M = 10^{(8.79C_{EQ}-1.52)};\ \Delta t_B = 10^{(8.84C_{EQ}-0.74)} \quad \text{(4A.1, 4A.2)}$$

where C_{EQ} is the carbon equivalent and considered as [*International Institute of Welding*].

The maximum volume fraction (V_{max}) undergoing solid-state phase transformations is estimated as a function of peak temperature (T_P) and percent of carbon content (C) in steel as

$$V_{MAX} = \begin{cases} 0 \text{ if } T_P \le A_1 \\ \left(\frac{T_P - A_1}{A_3 - A_1}\right) + \left(\frac{C}{0.83}\right)\left(\frac{A_3 - T_P}{A_3 - A_1}\right) \text{ if } A_1 < T_P \le A_3 \\ 1 \text{ if } T_P > A_3 \end{cases} \quad \text{(4A.3)}$$

where A_1 and A_3 are respectively the lower and upper critical temperatures for austenite formation and typically correspond to 1013 K and 1293 K, respectively for AISI 4140 steel. The volume fractions of martensite (V_M), bainite (V_B) and perlite-ferrtie (V_{FP}) were estimated next as

$$V_M = V_{max}\exp[-0.69(\Delta t/\Delta t_M)^2] \quad \text{(4A.4)}$$

$$V_B = V_{max}\exp[-0.69(\Delta t/\Delta t_B)^2 - V_M] \quad \text{(4A.5)}$$

$$V_{FP} = 1 - V_M - V_B \quad \text{(4A.6)}$$

where Δt was the total cooling time from 1073 K to 773 K. The Vickers hardness of different constituent phases were computed as

$$H_M = 127 + 949C + 27Si + 11Mn + 8Ni + 16Cr + 21\log(CR) \quad \text{(4A.7)}$$

$$H_B = -323 + 185C + 330Si + 153Mn + 65Ni + 144Cr + 191Mo + (89 + 53C - 55Si - 22Mn - 10Ni - 20Cr - 33Mo)\log(CR) \quad \text{(4A.8)}$$

$$H_{FP} = 43 + 223C + 53Si + 30Mn + 12.6Ni + 7Cr + 19Mo + (10 - 19Si + 4Ni + 8Cr + 130V)\log(CR) \quad \text{(4A.9)}$$

where (CR) is the computed cooling rate from 1073 K to 773 K. The net hardness (H) at any location is therefore estimated as

$$H = H_M V_M + H_B V_B + H_{FP} V_{FP} \quad \text{(4A.10)}$$

A sample calculation is shown in Table A1 for the estimation of hardness from the computed thermal history in FHPP of AISI 4140 steel. The calculations are corresponding to the thermal cycle shown in Figure 7(c) at force rate of 4.0 kN/s. Figure 4.13 shows cooling curves from Figure 4.7(c) superimposed on a CCT diagram for AISI 4140 steel (CORDOVILLA *et al.*, 2016).

Table 4.4 - Sample hardness calculation from computed temperature history.

C	**C_{EQ}**	**T_P**	**CR**	**Δt**
0.386	0.768	1473.18	107.14	2.8
Δt_M	**Δt_B**	**V_{MAX}**	**V_M**	**V_B**
169167.7	1113535	1.0	1.0	0.0
V_{FP}	**H_M**	**H_B**	**H_{FP}**	**H**
0	647.33	430.07	250.52	647.33

Source: Author.

Figure 4.13 - The cooling curves shown in Figure 4.7(c) are superimposed on CCT (continuous – cooling – transformation) diagram of AISI 4140 Steel.

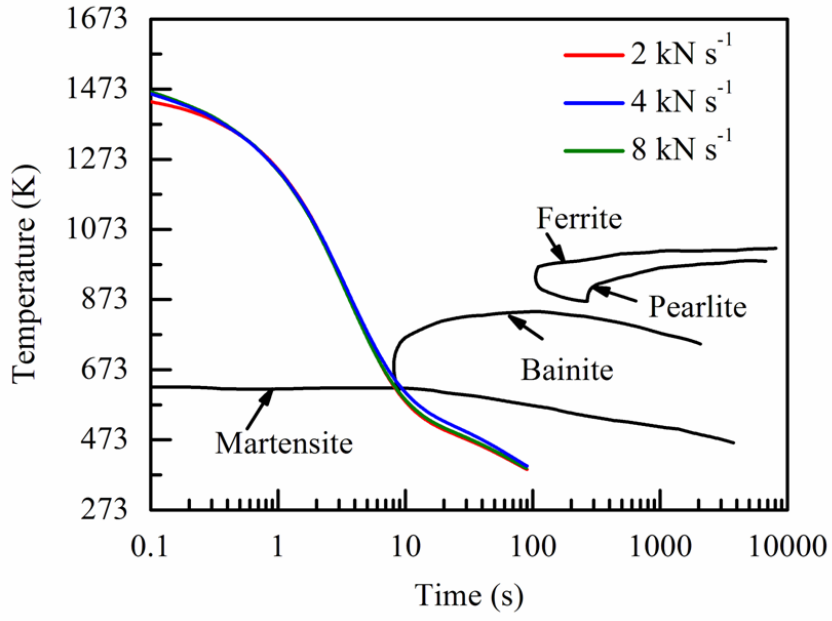

Source: Adapted from CORDOVILLA *et al.* (2016).

5 MATERIAL FLOW DURING FRICTION HYDRO-PILLAR PROCESSING

R Landell[1], L F Kanan[1], D Buzzatti[1], B Vicharapu[*2], A De[2], and T Clarke[1]

[1]Physical Metallurgy Laboratory (LAMEF) - PPGE3M/UFRGS, Porto Alegre, Brazil
[2]Indian Institute of Technology Bombay, Mumbai, India.
(*Corresponding author: buchibabu05@gmail.com)

Science and Technology of Welding and Joining
Volume 25, Jan 2020, No. 3, p. 228-234.
https://doi.org/10.1080/13621718.2019.1679963

Abstract

Friction hydro-pillar processing (FHPP) is a novel technique that involves solid state joining of an external plug onto a substrate by plastic deformation. A systematic investigation on material flow during FHPP is required but rarely reported. The present work reports a coupled theoretical and a three-dimensional X-ray computer tomography (XCT) based experimental study using a Ti-alloy as a tracer material to realize the material flow during FHPP of a AISI 4140 substrate. The cumulative results showed that the central portion of the plug deformed in a series of layer-wise shear planes. However, the plasticized material towards the outer area of the plug flowed through the clearance between the plug and the substrate with excess volume moving out as flash.

Keywords: Friction welding, Friction hydro-pillar processing, Friction taper plug welding, Material flow, X-ray computer tomography, Numerical simulation, Steel, Ti6Al4V.

5.1 INTRODUCTION

Friction hydro-pillar processing (FHPP) is a solid-state process, which involves joining of an external solid plug (referred to as stud) into a thick metallic base in order to repair cracks. FHPP is therefore finding increasing applications in oil, gas and power plant piping's, and parts and components in shipping fabrications (HATTINGH *et al.*, 2011; MEYER, 2003; YIN *et al.*, 2015). FHPP avoids common welding problems associated with melting of materials in weld zone and HAZ such as porosity, hydrogen embrittlement and residual stresses (MEYER, 2003; XU *et al.*, 2015). The process starts with the scraping of the crack and adjacent material from the damaged component by machining to form a shaped, blind hole with a base. A rotating, pre-shaped stud of similar chemical composition is then forced into the hole resulting in flow of plasticized stud material filling the hole. Subsequent coalescence of plasticized material with the substrate completes the process and brings back the damaged part to service. Figure 5.1 schematically shows three sequential steps of FHPP. The 'dwell stage' completes when the rotating stud touches the base of the crack opening in the substrate and marks the beginning of frictional heating along the stud-substrate interface. The plasticized material fills the hole in the 'burn-off stage'. The 'forging stage' begins with the stoppage of the stud rotation and application of additional force to facilitate consolidation of the plasticized material with the substrate (KANAN *et al.*, 2018; VICHARAPU *et al.*, 2017).

FHPP has been conceived initially with straight cylindrical shaped studs (MEYER, 2003; THOMAS; NICHOLAS, 1992). MEYER (2003) studied the material flow in FHPP of X65 pipeline steel using nickel as a tracer material that sheared-off during the burn-off stage due to overlapping and competing friction planes. The straight cylindrical shaped studs also showed inadequate mixing and lack of coalescence with the substrate (MEYER, 2003). Subsequent use of tapered cylindrical studs improved the filling of crack volumes and consolidation processes in FHPP of C-Mn steel, AISI 4140 and duplex stainless steels (UNS S31803) (KANAN *et al.*, 2018; MEINHARDT *et al.*, 2017; THOMAS; NICHOLAS, 1992; VICHARAPU *et al.*, 2017). The taper cylindrical studs also enhanced the rate of frictional heat generation (VICHARAPU *et al.*, 2017; ZHANG *et al.*, 2016). The lack of bonding defect could also be reduced by using pre-machines profiles of the existing cracks with chamfered edges (XU *et al.*, 2015). ZHANG *et al.* (2016) reported brittle microstructure of welded

region in underwater FHPP of X65 pipeline steel and attributed the same to high cooling rate. In summary, taper cylindrical studs and pre-machined cracks with chamfered edges provided improved joint in FHPP although the selection of appropriate processing conditions remained a challenge.

Figure 5.1 - Schematic illustrating (a) Initial stage, (b) dwell stage, (c) burn-off stage, (d) forging stage during friction stir hydro-pillar processing. Figure 1(f) shows schematically the variation of stud rotation, axial force, and stud burn-off at each stage.

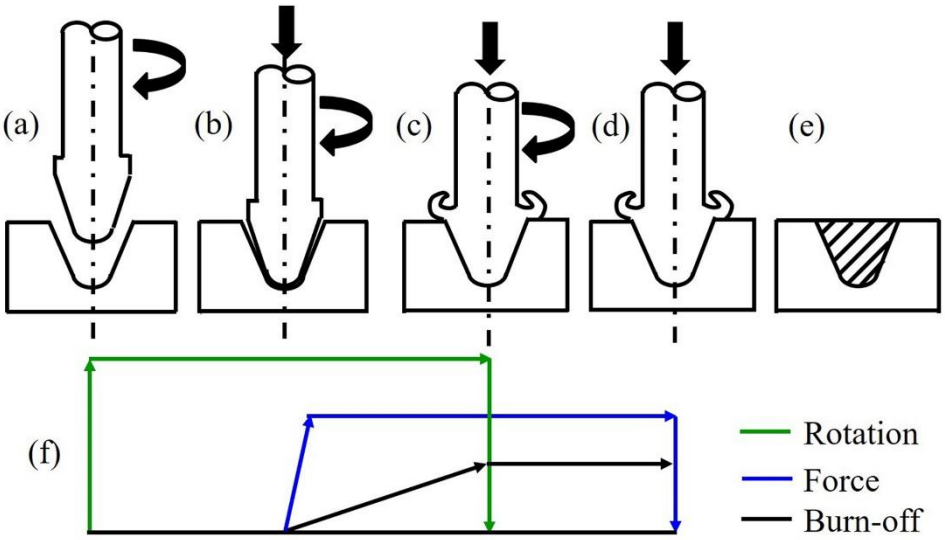

Source: Author.

The key processing conditions in FHPP include rotational speed of the stud, the peak force and the rate at which the force is applied on the stud, and the burn-off length of the stud. Kanan *et al.* (2018) could ensure filling of the crack-hole with plasticized material by a gentler increase in the stud force with time and using a longer dwell period in FHPP of AISI 4140 steel. The authors argued that a longer dwell period allowed adequate thermal softening and improved flow of plasticized stud material. In contrast, VICHARAPU *et al.* (2017) and ZHANG *et al.* (2016) noted that a higher axial force could reduce the overall processing time at the cost of high cooling rates and joint hardness. The effect of stud force on joint properties was found sensitive to the stud-hole geometries (HATTINGH *et al.*, 2011). CUI *et al.* (2014) opined that suitable combinations of stud rotational speed and force could improve the material flow and filling of crack-hole. However, these studies remained speculative about the influence of processing conditions and stud-hole geometry on material flow as direct investigation of material flow in FHPP was not attempted.

Attempts to examine material flow in FHPP using tracer material are reported in recent times while these were limited to the sectional views from the metallographic observations in two-dimensional planes only (MEYER, 2003; ZHANG *et al.*, 2016). The non-destructive X-ray computer tomography (XCT) technique has become a popular tool for acquisition of three dimensional (3D) images in processing of a wide range of engineering materials(MAIRE; WITHERS, 2014). XCT technology was employed for 3D visualization of porosity and volumetric welding defects (DIALAMI *et al.*, 2015; DINDA *et al.*, 2016), and distribution of intermetallic compounds in multi-material joining (KAR; SUWAS; KAILAS, 2018). Such studies are important in understanding the material flow during FHPP, but not available in open literature yet.

The present work aims at probing the stud material flow in FHPP of AISI 4140 with a tracer material and employing both XCT analysis and metallographic characterizations. Cylindrically shaped tracer material rods were inserted inside the stud to visualize the material flow explicitly. A finite element based fully coupled temperature-displacement analysis of FHPP is undertaken. The numerically computed peak temperature, material flow, flash volume and the weld shape are compared with the corresponding XCT and metallographic observations.

5.2 EXPERIMENTAL PROCEDURE

The FHPP experiments were conducted using a tapered stud and a thick substrate of AISI 4140 at the Physical Metallurgy Laboratory (LAMEF), Department of Metallurgical Engineering, Federal University of Rio Grande Do Sul (UFRGS), Brazil. Titanium alloy, Ti6Al4V was used as a tracer material due to its identical thermo-mechanical behavior with that of AISI 4140. Figure 5.2 shows the original stud and substrate geometry. Table 5.1 shows the chemical composition of the stud and substrate material. The nature of variation of flow stress of the stud and the tracer alloys are presented in **APPENDIX 5A**. The process conditions include the stud force, rotational speed and burn-off length of 35 kN, 7000 rpm and 7 mm, respectively. A set of trial experiments were conducted initially to ensure that the considered process condition could provide sound joints with adequate properties without any tracer material. Figure 5.2 shows two distinct locations for the placement of tracer rods of diameter 2 mm each inside the stud. It is presumed that the tracer material at the stud center would experience zero tangential velocity while that in the stud periphery

undergo the maximum tangential velocity. Three different experiments were conducted with (i) original stud, and (ii-iii) the stud with Ti6Al4V tracer at (ii) stud center, and (iii) 4 mm offset from the stud center.

Table 5.1 - Chemical composition of AISI 4140 steel.

C	Cr	Mo	Si	P	S	Mn	Ni
0.4	0.9	0.2	0.2	0.01	0.01	0.85	< 0.005

Source: Author.

X-ray computer tomography (XCT) analysis was performed on FHPP samples to study the material flow by a *Phoenix V/TOME/XM*© manufactured by *General Electric (GE)*©. The welded coupons were machined to 21 mm diameter cylindrical rods for XCT scanning according to the machine specifications (KRUMM; KASPERL; FRANZ, 2008). The samples were prepared with adequate care to maintain the FHPP joint at the central location of the rod. The voltage and current for the XCT analysis were 210 kV and 190 mA, respectively. The post-processing of XCT scans was performed using an open source software, '*Voreen Rendering',* from the University of Munster, Germany, to visualize the 3D distribution of tracer material (MEYER-SPRADOW *et al.*, 2009). The optical microscopy (OM) analysis was also performed on joint cross-sections (after etching with 5% Nital solution) to view the tracer material distribution. Two separate sample joints were made for XCT and OM analyses.

Figure 5.2 - Schematic view of (a) stud, (b) substrate with crack-hole, and (c-d) stud with the tracer rods - (c) tracer located centrally, and (d) tracer offset by 4 mm.

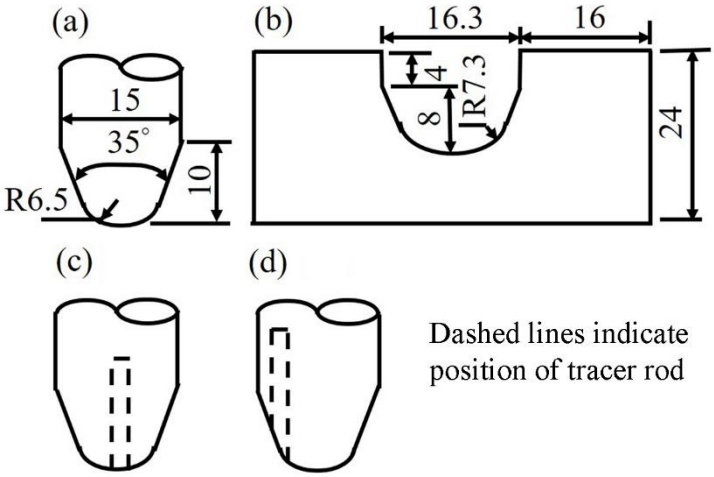

Source: Author.

5.3 NUMERICAL MODELING

The fully coupled temperature-displacement analysis of FHPP process is undertaken using the finite element software *ABAQUS*©/Standard V6.14 (DASSAULT SYSTÈMES SIMULIA CORP., 2014). The analysis considers the rate of heat generation due to frictional heating along the stud-substrate interface and plastic deformation of stud material. Figure 5.3(a) schematically shows the stud - substrate assembly with the stud modeled as an inverted taper cylindrical frustum with hemi-spherical end. Both the stud and substrate are considered as deformable and discretized with the special axisymmetric element (CGAX4HT) that includes temperature, displacement and twist degrees of freedom (DASSAULT SYSTÈMES SIMULIA CORP., 2012; MOAL; MASSONI, 1995). The twist degree of freedom allows the rotation and shear deformation in the out-of-plane direction. The governing heat transfer equation in two-dimensional cylindrical co-ordinate system can be stated as

$$\frac{1}{r}\frac{\partial}{\partial r}\left(kr\frac{\partial T}{\partial r}\right)+\frac{\partial}{\partial z}\left(k\frac{\partial T}{\partial z}\right)=\rho C_p\frac{\partial T}{\partial t} \tag{5.1}$$

where k, ρ, C_p T and t referred to the thermal conductivity, density, specific heat, and temperature and time variable, respectively. The boundary conditions can be expressed as

$$q_s - k\frac{\partial T}{\partial n} - h = 0 \tag{5.2}$$

where *h* is the convective heat transfer coefficient and q_S is the rate of frictional heat generation along the stud-substrate interface that is estimated as

$$q_S = \eta_h r \omega \tau \tag{5.3}$$

$$\tau = \begin{Bmatrix} \tau_y; & \tau_y \le P\mu \\ P\mu; & \tau_y > P\mu \end{Bmatrix} \tag{5.4}$$

where η_h is the fractional heat transferred to stud, *r* is the radial distance of a point from the stud axis, and μ, ω, *P* and τ_y refers to the co-efficient of friction, angular speed of stud, axial pressure on the stud and shear yield stress of stud material, respectively. The values of η_h and μ were considered as 0.5 and 0.3, respectively (KANAN *et al.*, 2018; VICHARAPU *et al.*, 2017). A lumped expression is used to estimate the convective heat loss from the surfaces as (BUCHIBABU; REDDY; DE, 2017; VICHARAPU *et al.*, 2019)

$$h = h_b \times (T - T_0) \tag{5.5}$$

where h_b = 10.0 W m^{-2} K^{-1}.

The analysis of mechanical response follows equation (5.6)

$$K \times U = F_M \tag{5.6}$$

where *K, U* and F_M are the stiffness matrix, displacement vector and the force vector due to mechanical work, respectively. The non-linearity in the mechanical analysis arises out of simultaneous displacement and rotation of the stud, and the temperature dependent thermo-physical properties of the stud and substrate material. The substrate bottom surface is constrained in all the directions. The stud is set to rotate with an angular velocity of '*ω*' in radial direction and displace in negative Z-direction during the stud burn-off.

Figure 5.3(b) shows the initial discretized stud-substrate assembly. The elements along the stud-substrate interface undergo large deformation as the modeling calculation continues through the burn-off stage. Significant distortion in element shapes tends to terminate the calculation process frequently and, intermittent re-meshing of heavily distorted elements is needed. A python based script was therefore written to undertake automatic remeshing of distorted elements and remapping of nodal solutions after each time-step (DASSAULT SYSTÈMES SIMULIA CORP., 2012). Figure 5.4(a-d) shows typical remeshed discretized geometry at four different time-steps during the stud burn-off period. The total number of elements were increased from 2982 to 3043 in Figure 5.4(a-d), respectively. The remeshing process

was undertaken sixty times to simulate 7 mm stud burn-off length for the given process conditions and stud-substrate geometry.

Figure 5.3 - Schematic of the (a) stud and substrate assembly, and. (b) initial mesh and (c) initial tracer locations (indicated in red color) at the beginning of the stud burn-off stage.

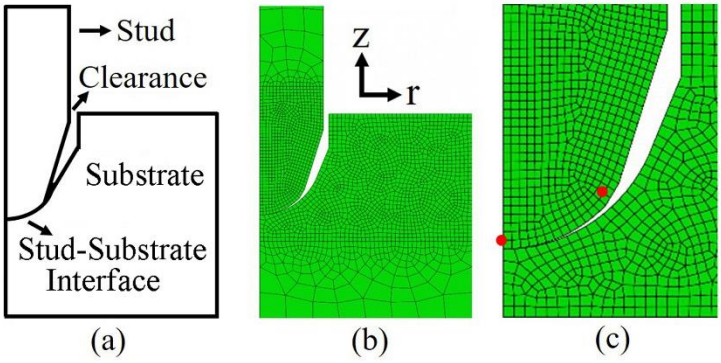

Source: Author.

The material flow during FHPP was modelled with the help of tracer particle tracking technique available in *ABAQUS*©. The tracer particles were located slightly above the stud surface inside the stud as shown in Figure 5.3(c) (highlighted with red color). Table 5.2 shows the thermo-physical properties and Table 5.3 presents the Johnson-Cook material constants for the estimation of flow stress of AISI 4140. The computed peak temperature, material flow, flash volume and the weld shape are compared with the corresponding experimental results.

Figure 5.4 - Re-meshed stud-substrate assembly at stud burn-off length (mm) of (a) 0.25, (b) 2, (c) 6, and (d) 7 during stud burn-off.

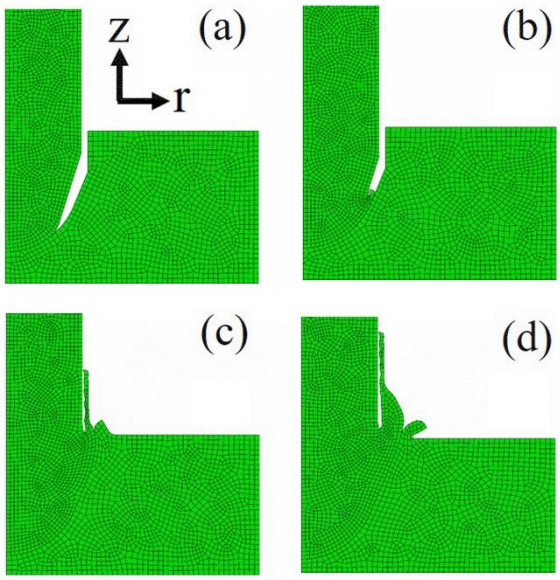

Source: Author.

Table 5.2 - Material properties of AISI 4140.

Density (kg/m^3)	7830
Solidus temperature (K)	1750
Thermal conductivity (W/mK)	$54.91-3.33e^{-2}\times T+1.0e^{-5}\times T^2$ for $T < 1200$ K 30.0 for $T \geq 1200$ K
Specific heat (J/kgK)	$361.55 + 1.13e^{-1}\times T +3.0e^{-4}\times T^2$ $300\ K \leq T \leq 1200\ K$ 607.0 for $T > 1200$ K

Source: KANAN *et al.* (2018).

Table 5.3 - Johnson-cook material model constants for AISI 4140.

Material	**A, MPa**	**B, MPa**	**C**	**m**	**N**	**T_M [K]**
AISI 4140	595	580	0.023	1.03	0.133	1820

where A: Initial yield stress, B: Hardening modulus, C: Strain rate dependency coefficient, m: Thermal softening coefficient, n: Strain-hardening coefficient, T_M: Melting temperature

Source: AGMELL; AHADI; STÅHL (2013).

5.4 RESULTS AND DISCUSSION

Figure 5.5 shows the joint cross-sections without (Figure 5.5) and with Ti6Al4V tracer materials [Figure 5.5(b, c)]. The joint in Figure 5.5(b) corresponds to the stud with a central tracer [Figure 5.2(c)] and that in Figure 5.5(c) with the tracer at a slightly offset location inside the stud [Figure 5.2(d)]. Figure 5.5(b) and (c) show the presence of Ti6Al4V tracer (brighter regions) at the center and along the stud-substrate interface, respectively. The joint cross-sections in Figure 5.5(a-c) show nearly identical profile with little presence of micro-crack and unbonded flash indicated by the red arrows and square boxes. The excess portion above the substrate surface is not part of the joint and removed later. A magnified view of the deformed tracer rod [Figure 5.5(b)] is shown in Figure 5.5(d) that manifests thin occasional overlapping layers of tracer material flowing along the stud-substrate interface. These layers are presumed as the representative shear layers. Similar layers were noted earlier in FHPP of X65 pipeline steel (MEYER, 2003). Figure 5.5(e) presents a zoomed view of Figure 5.5(c) with greater clarity depicting a radially outward, nearly uniform flow of tracer material through the stud-substrate interface with no presence of tracer in the central region of the interface. This indicates a similar nature of radially outward and then, upward flow of the plasticized stud material from its peripheral region through the stud-substrate interface. A further detailed visualization of the flow of tracer material is presented through the XCT analysis subsequently.

Figure 5.5 - Post weld macrographs of joint cross-sections with (a) no tracer, (b) Ti6Al4V tracer at center of the stud, (c) Ti6Al4V tracer at 4 mm away from the stud center. (d-e) show magnified views of (b-c), respectively.

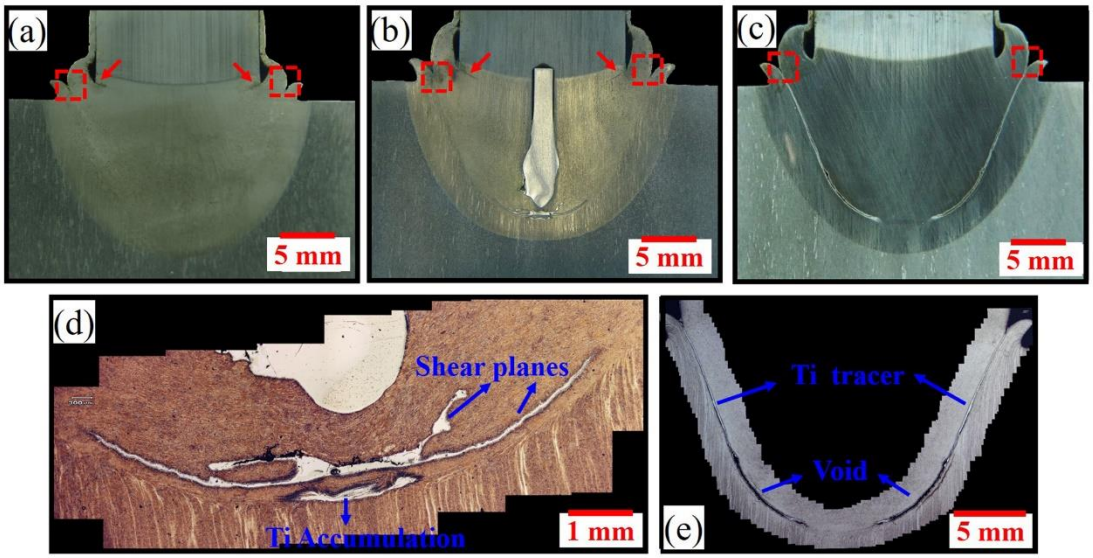

Source: Author.

Figure 5.6 show the XCT images of the joints when the Ti6Al4V tracer was at the stud center (Figure 5.6(a-b)) and slightly offset from the stud center [Figure 5.6(c-d)]. The fine dark particles in the processed zones indicate the distribution of tracer elements. Figure 5.6(b) shows a magnified view of Figure 5.6(a) near to the bottom of the deformed tracer rod. The intermittent ring patterns shown in Figure 5.6(b) indicate the typical shear layers that corroborates well with the metallographic observation [Figure 5.5(d)]. The offset placement of the tracer rod inside the stud led to the twisting of the rod as shown in Figure 5.6(c). A zoomed view of Figure 5.6(c) in Figure 5.6(d) indicates a radially outward flow of the tracer elements - upward through the stud-substrate interface as also observed in direct metallographic observation (Figure 5.5(e)). The Ti6Al4V tracer distributions in Figure 5.6(d) appear to be slightly intermittent that is attributed to insufficient resolution of the XCT setup to view finer tracer particles. The dark circular patterns along the top surface in Figure 5.6(a-c) depict unbonded flash material. The optical images (Figure 5.5) only shows the tracer distribution along the sectioned plane, whereas XCT analysis (Figure 5.6) reveals the tracer distribution in a 3D space, hence providing a better visualization. Overall, both the XCT and metallographic observations indicate that the central section of the stud deforms plastically in a series of shear planes and fills up the crack-hole. The

plasticized material towards the stud periphery flows through the stud-substrate interface thereby completing the filling process along the crack-hole profile.

Figure 5.6 - XCT images with Ti6Al4V tracer rod at the (a) stud center, and (b) a zoomed view of the same. (c) and (d) are with the Ti6Al4V tracer rod at a 4 mm offset from the stud center and its magnified view, respectively.

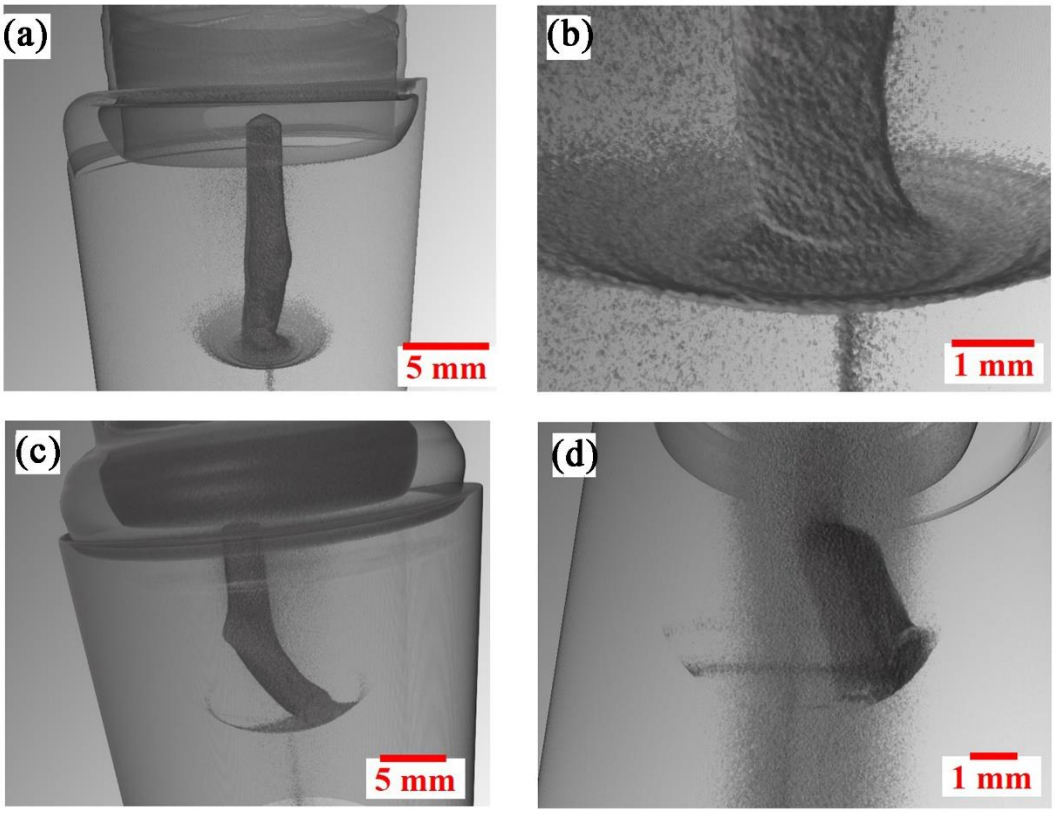

Source: Author.

5.4.1 Numerical results

Figure 5.7 shows the computed temperature iso-therms at four time-steps during the stud burn-off stage. An initial stud burn-off of around 0.5 mm occurred at a time instant of 0.9 s. The peak temperature at the end of the same time-instant reached to around 1025 K primarily due to frictional heat generation along the stud-substrate interface at the bottom of the stud [Figure 5.7(a)]. Only a little advancement of the plasticized stud material through the stud-substrate interface is noted in Figure 5.7(a). Figure 5.7(b) shows the temperature distribution and further advancement of plasticized stud material through the stud-substrate interface after the stud burn-off length reached to 2 mm. The corresponding time instant was 4 s. A rise in the peak

temperature to around 1275 K is noted in Figure 5.7(b). The increase in stud burn-off from 2 to 6 mm at a time instant of 14 s has led to the complete filling of the crack-hole with the peak temperature reaching around 1500 K along the stud-substrate interface. Further forcing the stud burn-off up to 7 mm has resulted in flash coming out from the crack-hole as shown in Figure 5.7(d). The computed peak temperatures reported in Figure 5.7 varies between 0.7 to 0.84 times the solidus temperature (T_S) of the workpiece material (ref Table 5.2). Previous studies on FHPP of AISI 4140 (KANAN *et al.*, 2018) and of ASTM A36 steel (VICHARAPU *et al.*, 2017) reported similar range of computed peak temperature. The stud burn-off length of around 5 mm filled the crack-hole completely and further introduction of the stud has led to flash [Figure 5.7(c-d)]. The computed results are checked further with the measured material flow and joint shape.

Figure 5.7 - Temperature isotherms at stud burn-off length (mm) of (a) 0.5, (b) 2, (c) 6, and (d) 7 during the stud burn-off stage.

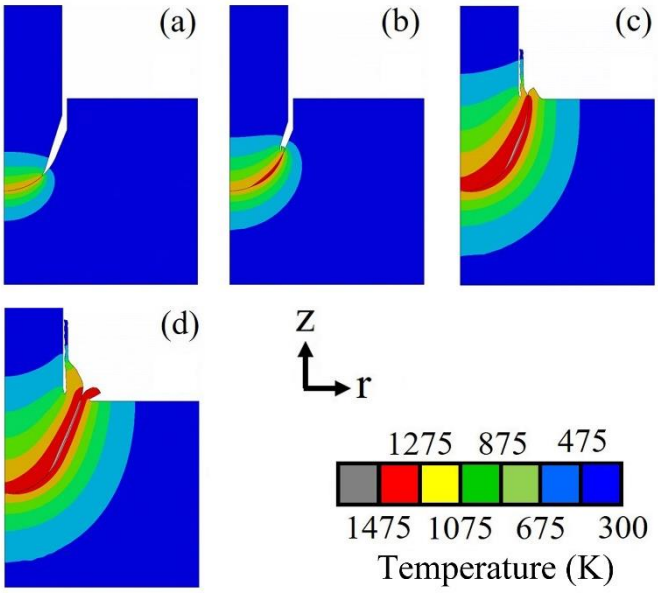

Source: Author.

5.4.2 Computed material flow and flash formation

Figure 5.8(a) and (b) show the step by step spatial evolution of tracer particle (highlighted in red color) as the FHPP process progresses with increase in the stud burn-off length. The initial and final tracer locations before and after the stud burn-off stage are indicated by the terms ‘Start’ and ‘End’, respectively. The locus of the tracer

particle shown in Figure 5.8(a) depict the movement of the shear plane that is in line with both the XCT and metallographic observations [ref. Figure 5.5(d) and Figure 5.6(b)]. Likewise, the computed tracer distribution shown in Figure 5.8(b) from the offset placement of the tracer agreed well with the corresponding experimentally measured results [ref. Figure 5.5(e) and Figure 5.6(d)]. The model is therefore considered fairly representative in realizing the flow and expelling of stud material as flash through stud-substrate interface. The model is validated further with the weld joint shape and flash size. Figure 5.8(c) further illustrates the flow of material from the central and peripheral portions of the stud as hypothesized based on the experimental investigation and modeling calculations. The material near the central portion of the stud would deform in a series of shear planes one upon the other, which are highlighted with the red color dashed lines in Figure 5.8(c). This plastically deformed material remains inside the processed zone. The plastic flow of material from the tapered surface of the stud flown along the stud-hole contact interface in radially outward and upward direction and eventually the excess material expels as flash as shown in Figure 5.8(c).

Figure 5.8 - Distribution of tracer particles from (a) stud center and (b) 4 mm away from the stud center at the end of stud burn-off stage; and (c) schematic of material flow during FHPP.

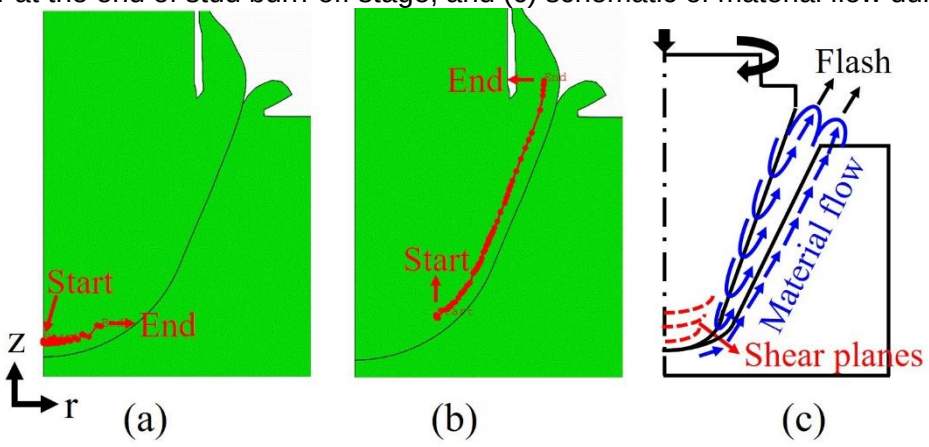

Source: Author.

Figure 5.9(a-b) compare the measured profile of flash and joint cross-section with the corresponding computed results at two different process conditions. The measured joint cross-section in Figure 5.9(a) is from Figure 5.5(a) while that in Figure 5.9(b) is considered from literature (KANAN *et al.*, 2018). In Figure 5.9(a-b), the original stud-substrate boundary is shown by the white dashed line that agrees well with the corresponding simulated flow of the tracer particles in both the cases. The

profiles of the flash exiting out of the stud-substrate interface also indicate a fair correspondence between the model predictions and measures ones.

The material flow during FHPP of AISI 4140 was studied using Ti46Al4V as a tracer material. The tracer material distribution in FHPP joint was characterized by both XCT and metallographic analysis. A fully coupled temperature-displacement model was used to examine the evolution of material flow and temperature distribution as the externally rotating stud is introduced and forced to flow plastically to fill the crack-hole during the process. The XCT is proved to be a promising tool to visualize 3D material flow in typical solid-state joining processes involving flow of plasticized material. The experimental and numerical approaches presented here are fairly novel in nature for the analysis of FHPP that is increasing considered for joining of an external stud to a substrate for repairing of three-dimensional cracks.

Figure 5.9 - Computed and measured joint cross-sections and flash profiles at two different combinations of stud rotational speed (rpm), stud force (kN) and stud burn-off (mm) of (a) (8000, 35, 7.0), and (b) (5000, 25, 6.5). Macrograph shown in Fig 9(b) is considered from independent literature (KANAN *et al.*, 2018).

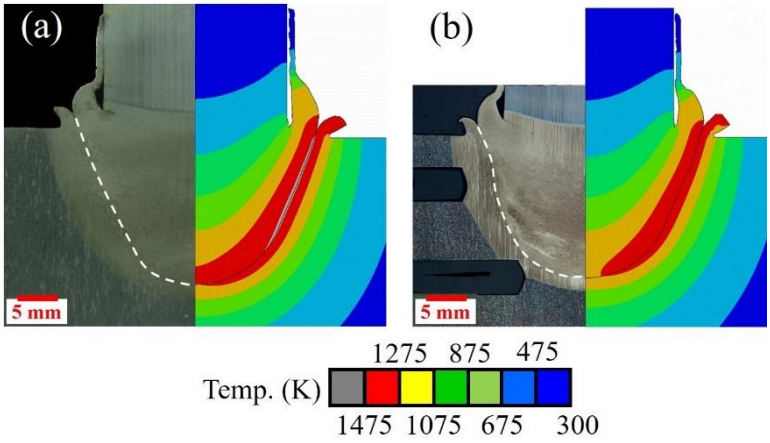

Source: Author.

5.5 CONCLUSIONS

A systematic investigation on material flow in friction hydro-pillar processing is presented here based on novel experimental observation and comprehensive numerical modeling The following conclusions are arrived at as a part of this detailed investigation.

- The material near the central portion of the stud plastically deformed in a series of shear planes one upon the other and this material remains inside the processed zone.
- The plastic flow of stud material from the taper surface flows in a radially outward and upward direction along the stud-hole interface, and eventually expelling as flash at the end of the stud burn-off.
- The thermal-displacement model developed in this study is first of its kind in friction hydro-pillar processing literature and the computed peak temperature, material flow distribution, weld joint shape, and flash size and shape are fairly agreed well the corresponding X-ray computer tomography and metallographic results.

Acknowledgements

The authors would like to thank the research support of Petrobras, ANP (Brazilian Agency for Petroleum and Energy) and General Electric. The authors are thankful to the late Prof. T.R. Strohaecker (LAMEF/PPGE3M), whose presence and wisdom will be profoundly missed.

APPENDIX 5A

Table 5.4 provide the Johnson-Cook model constants for Ti-6Al-4V. Figure 5.10 compares the flow stress between Ti-6Al-4V and the AISI 4140 steel as function of (a) temperatures, and (b) equivalent plastic strains. Figure 5.10 shows that the flow stress of AISI 4140 and Ti6Al4V is reasonably close to each-other.

Table 5.4 - Johnson-cook model constants for tracer.

Material	**A, MPa**	**B, MPa**	**C**	**M**	**N**	**T_M [K]**
Ti6Al4V	862.5	331.2	0.012	0.8	0.34	1941

Source: (MEYER; KLEPONIS, 2001).

Figure 5.10 - A comparison of flow stresses for AISI 4140 and Ti6Al4V as function of (a) temperatures, and (b) equivalent plastic strains.

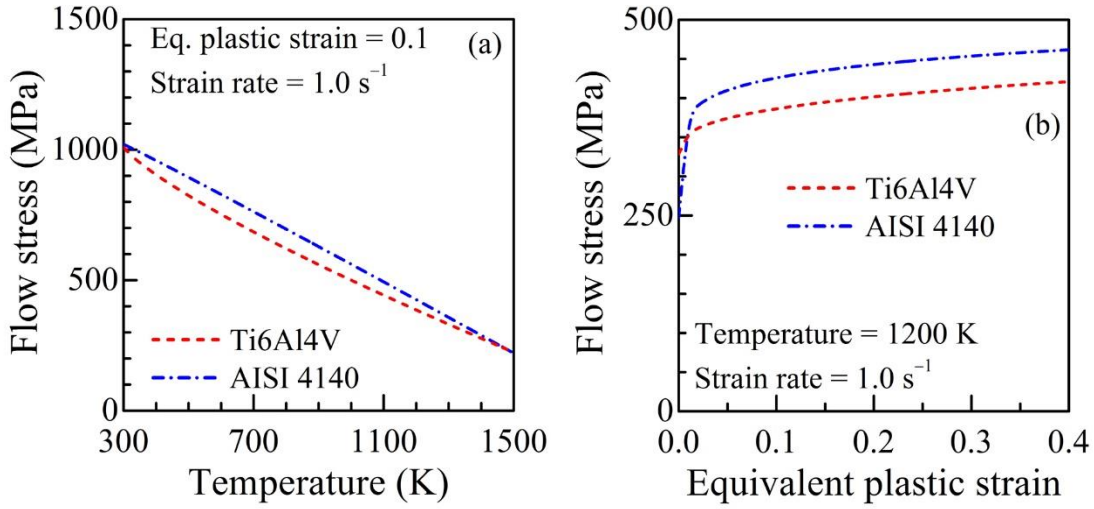

Source: Adapted from (AGMELL; AHADI; STÅHL, 2013; MEYER; KLEPONIS, 2001).

6 CONCLUDING REMARKS

This PhD thesis synthesizes three distinct articles that contribute significantly to the field of friction hydro-pillar processing (FHPP) in thick-walled structures. These articles collectively provide valuable insights into various aspects of FHPP, including temperature field computation, hardness distribution estimation, void and defect reduction, material flow characterization, and the development of numerical models.

The conclusions of the first article (VICHARAPU *et al.*, 2017) can be summarized as:

1. A methodology to calculate the temperature field and estimate the hardness distribution in the repair of thick structures through FHPP welding was presented for the first time in the literature;
2. Longer processing times decrease the force required for FHPP welding of ASTM A36 steel, but result in a higher peak temperature and smoother temperature gradient, leading to a more uniform hardness distribution;
3. The calculated thermal cycles and hardness distribution were similar to those experimentally measured for the conditions tested in FHPP welding on ASTM A36 steel;

The second paper (KANAN *et al.*, 2018) conclusions:

4. The strength rate was considered one of the main variables in the FHPP entry process for the first time in the literature;
5. Higher force ratings decrease processing time during the first stage of FHPP welding on AISI 4140 steel and increase the formation of crack-like defects at the bottom of the weld due to inadequate thermal gradients and localized discontinuities;
6. A slow force rate in the first stage of FHPP welding on AISI 4140 steel showed a defect-free weld;
7. All conditions tested in FHPP welding on AISI 4140 steel showed martensite formation in the processed zone, and a transient heat transfer model was used to simulate the thermal profiles and estimate the material hardness with reasonable accuracy;
8. The fully validated heat transfer model can be used further for an estimation of the temperature distribution, structure and properties of the joint;

The third article (LANDELL *et al.*, 2019) main conclusions are:

9. The material is plastically deformed in a series of stacked shear planes in the region closest to the axis of the pin, and this material remains within the processed zone;
10. The material flow on the taper surface flows along the weld interface, towards the outside of the hole, eventually being expelled as flash during consumption;
11. The thermo-mechanical model developed in this study calculated the peak temperature, the material flow trajectory, the final shape of the solder joint and the size and shape of the flash consistently to the results of computed tomography and corresponding metallographic analyses.

In conclusion, these three articles collectively provide a comprehensive overview of FHPP, addressing critical aspects such as temperature control, defect reduction, and material flow characterization. The findings from these articles offer valuable insights that can inform FHPP process optimization and contribute to the advancement of this important technology in the field of materials processing. This thesis synthesizes and integrates these findings, improving the understanding of FHPP and its potential applications in various industries.

7 FUTURE WORK

The research conducted in this thesis has shed light on various aspects of friction hydro-pillar processing (FHPP) and has contributed significantly to our understanding of this innovative technology. However, as with any research, there are numerous avenues for future work and exploration that can further enhance our knowledge and extend the practical applications of FHPP.

7.1 APPLICATIONS OF THE THERMOMECHANICAL MODEL

One of the primary areas for future work is the exploration of the thermomechanical model developed in chapter 5. This model has shown promise in predicting temperature profiles and material flow accurately during FHPP. Future research efforts can focus on the following aspects:

- Residual Stresses
  - Investigate the model's capability to predict residual stresses in the processed zone, providing valuable insights into the structural integrity of FHPP components.
- Grain Refining and Deformation History
  - Explore the relationship between FHPP parameters and grain refinement within the processed material.
  - Develop a comprehensive understanding of the deformation history of the material during FHPP.
- Hardness Calculation with Grain Refinement
  - Investigate the influence of grain refinement on hardness distribution.
  - Develop a method for accurately calculating hardness when grain refinement is a prominent factor.
- Geometry Variation and Flow Change
  - Analyze how variations in workpiece geometry affect material flow during FHPP.
  - Examine the correlation between geometry changes and alterations in material flow behavior.

7.2 METHODS DEVELOPMENT

In addition to further exploring the thermomechanical model, it is essential to expand the applicability of FHPP across various materials and operational conditions:

- Repeat Procedure with Other Materials
  - Conduct FHPP experiments with a wide range of materials to assess the model's adaptability and reliability.
  - Compare and contrast FHPP outcomes for different materials to identify material-specific trends and challenges.
- Repeat Procedure with Underwater Applications
  - Investigate the feasibility and effectiveness of FHPP in underwater environments.
  - Assess the impact of water on material flow, temperature distribution, and FHPP outcomes.

7.3 IDENTIFYING POTENTIAL APPLICATIONS AND INDUSTRIES OF INTEREST

Perhaps the most crucial aspect of future work is the identification of potential applications and industries where FHPP can bring about transformative changes. This entails interdisciplinary research and collaboration with industry partners:

- Establish collaborative partnerships with industries that could benefit from FHPP, such as aerospace, automotive, and construction.
- Conduct market research to identify niche areas within various industries where FHPP can address specific challenges and needs.
- Perform feasibility studies to assess the economic viability and practicality of implementing FHPP in specific applications.
- Customization and Optimization: Tailor FHPP parameters and procedures to suit the unique requirements of different industries and applications.

In summary, this chapter underscores the promising avenues for future FHPP research and application, signifying its potential to drive innovation and establish itself as a transformative technology within the realm of materials processing.

8 REFERENCES

AGMELL, Mathias; AHADI, Aylin; STÅHL, Jan Eric. The link between plasticity parameters and process parameters in orthogonal cutting. **Procedia CIRP**, vol. 8, p. 224–229, 2013. Available at: http://dx.doi.org/10.1016/j.procir.2013.06.093.

AMAVISCA C. V. **Estudo das tensões residuais em juntas soldadas obtidas através da soldagem por fricção com pino consumível no aço AISI H13**. 2019. 1–114 f. - UFRGS, Porto Alegre, RS, Brasil, 2019. Available at: https://www.lume.ufrgs.br/bitstream/handle/10183/200586/001103475.pdf?sequence=1&isAllowed=y.

AMERICAN WELDING SOCIETY. **Welding Handbook Eighth Edition - Volume 2: Welding Processes**. 8th. ed. Miami: AWS, 1991.

ASM INTERNATIONAL HANDBOOK COMMITTEE. **ASM Handbook - Properties and Selections - Irons Steels and High and Performance Alloys**. Materials Park, OH: ASM International, 2008. vol. 1

ASM INTERNATIONAL HANDBOOK COMMITTEE. **ASM Handbook - Welding Brazing and Soldering**. 10th. ed. Materials Park, OH: ASM International, 1993. vol. 6

ASM INTERNATIONAL HANDBOOK COMMITTEE. **Heat Treating**. Materials Park, OH: ASM International, 1991. vol. 4

ASTM INTERNATIONAL. **E230/E230M-17 - Standard Specification for Temperature-Electromotive Force (emf) Tables for Standardized Thermocouples**. West Conshohocken, United States: ASTM International, 2017.

BUCHIBABU, V.; REDDY, G. M.; DE, A. Probing torque, traverse force and tool durability in friction stir welding of aluminum alloys. **Journal of Materials Processing Technology**, Amsterdam, vol. 241, p. 86–92, 2017.

BULBRING, D. L.H. *et al.* Friction Hydro Pillar Process as an alternative repair technology for creep evaluation sites on thick-walled 10CrMo910 creep-resistant steel structures. **Journal of the Southern African Institute of Mining and Metallurgy**,

Magaliesburg, South Africa, vol. 113, no. 2, p. 129–136, 2013.

BUZZATTI, Diogo Trento *et al.* Friction Hydro Pillar Processing: Characteristics and Applications. **Soldagem & Inspeção**, vol. 20, no. 3, p. 287–299, 2015.

CHLUDZINSKI, M. *et al.* Fracture toughness of Friction Hydro-Pillar Processing welding in C-Mn steel. **Materials and Design**, Amsterdam, vol. 33, no. 1, p. 340–344, 2012. Available at: http://dx.doi.org/10.1016/j.matdes.2011.07.056.

CORDOVILLA, Francisco *et al.* Numerical/experimental analysis of the laser surface hardening with overlapped tracks to design the configuration of the process for Cr-Mo steels. **Materials and Design**, Amsterdam, vol. 102, p. 225–237, 2016. Available at: http://dx.doi.org/10.1016/j.matdes.2016.04.038.

CUI, Lei *et al.* Friction taper plug welding for S355 steel in underwater wet conditions: Welding performance, microstructures and mechanical properties. **Materials Science and Engineering A**, Amsterdam, vol. 611, p. 15–28, 2014. Available at: http://dx.doi.org/10.1016/j.msea.2014.04.087.

DASSAULT SYSTÈMES SIMULIA CORP. Chapter 6.5– Heat transfer and thermal-stress analysis. *In*: ABAQUS ANALYSIS USER'S MANUAL. Providence: Dassault Systèmes, 2014. p. 324–361.

DASSAULT SYSTÈMES SIMULIA CORP. Example number 1.3.18 Inertia friction welding. *In*: ABAQUS EXAMPLE PROBLEMS GUIDE. Providence: Dassault Systèmes, 2012. p. 484–500.

DE, Amit. Finite element modelling of resistance spot welding of aluminium with spherical tip electrodes. **Science and Technology of Welding and Joining**, London, vol. 7, no. 2, p. 119–124, 2002.

DE ALBUQUERQUE, Victor H.C. *et al.* Effect of nonmetallic inclusion and banding on the success of the two-layer temper bead welding technique. **Materials and Design**, vol. 30, no. 4, p. 1068–1074, 2009. Available at: http://dx.doi.org/10.1016/j.matdes.2008.06.056.

DE, A.; BHADESHIA, H. K.D.H.; DEBROY, T. Friction stir welding of mild steel: Tool

durability and steel microstructure. **Materials Science and Technology**, London, vol. 30, no. 9, p. 1050–1056, 2014.

DE LIMA LESSA, Cleber Rodrigo *et al.* Microstructural behavior of SAF 2205 duplex stainless steel welded by Friction Hydro Pillar processing. **Materials Research**, São Paulo, vol. 19, no. 4, p. 928–936, 2016.

DIALAMI, N. *et al.* Material flow visualization in friction stir welding via particle tracing. **International Journal of Material Forming**, Paris, vol. 8, no. 2, p. 167–181, 2015.

DINDA, Soumitra Kumar *et al.* 3D imaging and quantification of porosity in electron beam welded dissimilar steel to Fe-Al alloy joints by X-ray tomography. **Materials and Design**, Amsterdam, vol. 96, p. 224–231, 2016. Available at: http://dx.doi.org/10.1016/j.matdes.2016.02.010.

FUJII, Hidetoshi *et al.* Friction stir welding of carbon steels. **Materials Science and Engineering A**, Amsterdam, vol. 429, no. 1–2, p. 50–57, 2006.

HARTLEY, P. J. Friction plug weld repair for the space shuttle external tank. **Welding and Metal Fabrication**, vol. 9, p. 6–8, 2000.

HATTINGH, D. G. *et al.* Damage assessment and refurbishment of steam turbine blade/rotor attachment holes. **Theoretical and Applied Fracture Mechanics**, vol. 83, p. 125–134, 2016. Available at: http://dx.doi.org/10.1016/j.tafmec.2015.11.001.

HATTINGH, D. G. *et al.* Friction processing as an alternative joining technology for the nuclear industry. **Journal of the Southern African Institute of Mining and Metallurgy**, vol. 115, no. 10, p. 903–912, 2015.

HATTINGH, D. G. *et al.* Process parameter influence on performance of friction taper stud welds in AISI 4140 steel. **Materials and Design**, vol. 32, no. 6, p. 3421–3430, 2011. Available at: http://dx.doi.org/10.1016/j.matdes.2011.02.001.

HOWSE, D.; LUCAS, W.; THOMAS, W. Novel joining techniques for repair in the power generation industry. *In*: , 2002, Point Clear. **EPRI Welding and Repair Technology for Power Plants Conference**. Point Clear: TWI, 2002. p. 1–18. Available at: http://www.twi.co.uk/technical-knowledge/published-papers/novel-

joining-techniques-for-repair-in-the-power-generation-industry-june-2002/.

ION, J.C.; EASTERLING, K.E.; ASHBY, M.F. A SECOND REPORT ON DIAGRAMS OF MrCROSTRU ~ T ~ RE AND HARDNESS FOR HEAT-AFFECTED ZONES. **Acta metall**, London, vol. 32, no. 11, p. 1949–1962, 1984.

KANAN, Luis Fernando *et al.* Friction hydro-pillar processing of a high carbon steel: Joint structure and properties. **Metallurgical and Materials Transactions B: Process Metallurgy and Materials Processing Science**, vol. 49, no. 2, p. 699–708, 2018. Available at: https://doi.org/10.1007/s11663-018-1171-5.

KAR, Amlan; SUWAS, Satyam; KAILAS, Satish V. Two-pass friction stir welding of aluminum alloy to titanium alloy: A simultaneous improvement in mechanical properties. **Materials Science and Engineering: A**, Amsterdam, vol. 733, p. 199–210, 2018. Available at: https://doi.org/10.1016/j.msea.2018.07.057.

KOU, Sindo. **Welding Metallurgy**. 1st ed.ed. New York: Wiley, 1987.

KRUMM, M.; KASPERL, S.; FRANZ, M. Reducing non-linear artifacts of multi-material objects in industrial 3D computed tomography. **NDT and E International**, Amsterdam, vol. 41, no. 4, p. 242–251, 2008.

LAKHKAR, Ritesh S.; SHIN, Yung C.; KRANE, Matthew John M. Predictive modeling of multi-track laser hardening of AISI 4140 steel. **Materials Science and Engineering: A**, vol. 480, no. 1–2, p. 209–217, 2008.

LANDELL, Renan *et al.* Material flow during friction hydro-pillar processing. **Science and Technology of Welding and Joining**, vol. 25, no. 3, p. 228–234, 2019. Available at: https://doi.org/10.1080/13621718.2019.1679963.

LESSA, Cleber Rodrigo de Lima *et al.* Friction Hydro-Pillar Processing and Tungsten Inert Gas Welding of a Duplex Stainless Steel. **Materials Science and Technology (United Kingdom)**, vol. 35, no. 10, p. 1161–1172, 2019. Available at: https://doi.org/10.1080/02670836.2019.1613801.

LI, Wukai *et al.* Numerical simulation of temperature field and prediction of microstructure in friction hydro pillar processing. **Journal of Materials Processing**

Technology, vol. 252, no. September 2017, p. 370–380, 2018. Available at: http://dx.doi.org/10.1016/j.jmatprotec.2017.10.001.

MAIRE, E.; WITHERS, P. J. Quantitative X-ray tomography. **International Materials Reviews**, vol. 59, no. 1, p. 1–43, 2014.

MEINHARDT, C. P. *et al.* Evaluation of friction hydro-pillar processing welding in duplex stainless steels (UNS S31803). **Journal of Materials Processing Technology**, vol. 246, p. 158–166, 2017. Available at: http://dx.doi.org/10.1016/j.jmatprotec.2017.03.010.

MEYER-SPRADOW, Jennis *et al.* Voreen: A rapid-prototyping environment for ray-casting-based volume visualizations. **IEEE Computer Graphics and Applications**, New Jersey, vol. 29, no. 6, p. 6–13, 2009.

MEYER, A. **Friction Hydro Pillar Processing – Bonding Mechanism and Properties**. 2003. 132 f. - Technischen Universität Carolo-Wilhelmina zu Braunschweig, 2003.

MEYER, Hubert W.; KLEPONIS, David S. Modeling the high strain rate behavior of titanium undergoing ballistic impact and penetration. **International Journal of Impact Engineering**, Amsterdam, vol. 26, no. 1–10, p. 509–521, 2001.

MOAL, A.; MASSONI, E. Finite element simulation of the inertia welding of two similar parts. **Engineering Computations**, West Cross, Swansea, UK, vol. 12, no. 6, p. 497–512, 1995.

NANDAN, R. *et al.* Three-dimensional heat and material flow during friction stir welding of mild steel. **Acta Materialia**, vol. 55, no. 3, p. 883–895, 2007.

NICHOLAS, E.D. Friction Processes. **Welding in the World**, vol. 47, no. 11, p. 2–9, 2003. Available at: https://link.springer.com/article/10.1007/BF03266402.

PAULY, D *et al.* **A preliminary study on the application of Friction Welding in structural repairsGKSS reports**. Geesthacht: GKSS, 1998.

PRIME, M. B. Cross-sectional mapping of residual stresses by measuring the surface contour after a cut. **Journal of Engineering Materials and Technology,**

Transactions of the ASME, vol. 123, no. 2, p. 162–168, 2001.

ROTHMAN, M.F. **High temperature property data: ferrous alloys**. 2nd ed.ed. Metals Park, OH: ASM International, 1989.

SILVA, Cleiton C. *et al.* Evaluation of AISI 4140 steel repair without post-weld heat treatment. **Journal of Materials Engineering and Performance**, vol. 18, no. 3, p. 324–331, 2009.

THOMAS, Wayne Morris *et al.* **Friction forming - WO1993004813A1**. Concessão: 1993.

THOMAS, W.M.; NICHOLAS, E.D. TWI, Leading Edge. Friction hydro pillar processing. **TWI Connect Press**, 1992. Available at: www.twi.co.uk.

UNFRIED S., J. *et al.* Study of microstructural evolution of friction taper plug welded joints of C-Mn steels. **Science and Technology of Welding and Joining**, vol. 15, no. 6, p. 506–513, 2010.

VICHARAPU, Buchibabu *et al.* An investigation on friction hydro-pillar processing. **Science and Technology of Welding and Joining**, vol. 22, no. 7, p. 555–561, 2017. Available at: http://dx.doi.org/13621718.2016.1274849.

VICHARAPU, B. *et al.* Probing Tool Durability in Stationary Shoulder Friction Stir Welding. *In*: , 2019, Cham. **Friction Stir Welding and Processing X. The Minerals, Metals and Materials Series**. Cham: Springer, 2019. p. 91–98.

XU, Y. C. *et al.* Numerical simulation of the effects of various stud and hole configurations on friction hydro-pillar processing. **International Journal of Mechanical Sciences**, vol. 90, p. 44–52, 2015.

YEH, Felipe Wu Tzong *et al.* Evaluation of discontinuities in a36 steel repairs with friction hydro pillar processing using different axial forces. **ISIJ International**, vol. 53, no. 12, p. 2269–2271, 2013.

YIN*, Yayun *et al.* Investigation on welding parameters and bonding characteristics of underwater wet friction taper plug welding for pipeline steel. **International Journal of Advanced Manufacturing Technology**, vol. 81, no. 5–8, p. 851–861, 2015.

YIN, Yayun *et al.* Material flow influence on the weld formation and mechanical performance in underwater friction taper plug welds for pipeline steel. **Materials and Design**, vol. 88, p. 990–998, 2015. Available at: http://dx.doi.org/10.1016/j.matdes.2015.09.123.

ZHANG, Xunda *et al.* Improving bonding quality of underwater friction stitch welds by selecting appropriate plug material and welding parameters and optimizing joint design. **Materials and Design**, vol. 91, p. 398–410, 2016. Available at: http://dx.doi.org/10.1016/j.matdes.2015.11.114.